2.2 Experimental Study of Thermocapillary Flow in the Half-Zone Liquid Bridge of Low Prandtl Number Fluid

NASDA Space Utilization Research Center

EXPERIMENTAL STUDY OF THERMOCAPILLARY FLOW IN THE HALF-ZONE LIQUID BRIDGE OF LOW PRANDTL NUMBER FLUID

Katsuhiko Takagi [1], Masahiko Ohtaka [1], Hidesada Natsui [2], Tatsuya Arai [1], and Shinichi Yoda [1]

[1] National Space Development Agency of Japan, Sengen 2-1-1, Tsukuba-city, Ibaraki 305-8505, Japan
[2] Advanced Engineering Services Co. Ltd., Takezono 1-6-1, Tsukuba-city, Ibaraki 305-0032, Japan

Oscillatory thermocapillary flow of low Prandtl number fluid in the half-floating zone was experimentally studied under normal gravity. Measurement technique in surface temperature of a liquid bridge of tin as a test fluid was developed. Theoretical investigation of radiation energy from molten tin showed that PbS photo detector can measure proper wavelength range with high radiation energy, combined with use of CaF_2 optical pass filter. It was confirmed that the selected radiation thermometer had temperature resolution that was smaller than amplitude of temperature fluctuation of oscillatory flow.

The new measuring technique made it possible to observe surface temperature fluctuations successfully by using the ex-chamber in which CaF_2 optical pass filter has not been installed. The periodic fluctuation continued approximately 100sec, then damped gradually, suggesting that reduction in temperature dependence of surface tension be caused by oxidation of molten surface. A temperature difference of 7.6K was observed for onset of the periodic flow, which was almost good agreement with the numerical result with 7.1K. It should be noted here the second bifurcation point, which has never observed yet, could be detected by the present experiments.

Considerations for surface science of tin led us to design of unique experiment apparatus where clean surface of molten tin was able to obtain and sustain during an experiment. Ar^+ ion etching method was applied to remove residual surface oxides, and effectiveness of the etching was confirmed by the installed ion gun that was designed for surface cleaning. Prevention of further oxidation under vacuum condition of about 10^{-6}Pa during one experiment was experimentally verified by *in situ* measurements of surface tension of molten tin.

Novel visualization technique (3D-UV) of flow field measurements for liquid metals using ultrasonic transducer with high heat resistance is currently under development for the experiments. It was concluded that the first bifurcation point could be detected precisely by 3D-UV technique with the consideration of the experimentally predicted performances such as a resolution, a minimum size of a tracer, and a signal processing method. 3D-UV can visualize flow field of the liquid bridge in which the aspect ratio is a range of 2.3 (a=1.5mm) to 0.8 (a=5mm). The visualization technique requires development of unique balloon-like tracer also. It was confirmed that the balloon tracer with good sphericity could be actually manufactured by electroless plating of Ni over surface of Shirasu-balloon, which is an expanded volcanic particle, subsequently by electrolysis plating of Fe.

1. INTRODUCTION

It is well known that thermocapillary flow has an undesirable effect on the crystal growth of semi-conductors by the floating zone (FZ) method, which leads to striation of the dopant induced by oscillatory thermocapillary flow in melt.

Many experimental researches, numerical simulations, and theoretical analyses have been conducted on thermocapillary flow in the half zone-liquid bridge, using simulated molten material in the FZ configuration. These previous researches proved that flow and temperature fields were governed by dimensionless parameter of Marangoni (Ma) or Reynolds (Re) number defined as following:

$$\mathrm{Ma} = \frac{|\sigma_T|\Delta TL}{\mu\alpha} \qquad (1\text{-}1),$$

$$\mathrm{Re} = \mathrm{Ma}/\mathrm{Pr} \qquad (1\text{-}2),$$

where, σ_T is temperature gradient of surface tension, ΔT a temperature difference between hot and cold disks, L a characteristic length of the fluid, μ dynamic viscosity, α thermal diffusivity, and Pr Prandtl number of the fluid. In this study, a radius (a) of the liquid bridge is used as a characteristic length because of easy comparison with the numerical works done by Prof. Imaishi et al. (see chapter 3.1).

Thermocapillary flow would be transitioned from axisymmetric steady to 3D oscillatory flow as the temperature difference increased. Figure 1-1 shows an overview of the transition behavior of thermocapillary flow. In high Prandtl number fluids, it was proved that a transition from axisymmetric to 3D oscillatory occurs beyond the onset point. On the other hand, it was numerically predicted that thermocapillary flow in a low Prandtl number had two transition points: that is, a flow transition from axisymmetric to 3D steady will occur at the first bifurcation point, and a transition from 3D steady to 3D oscillatory at the second bifurcation. The prediction needs to be proven experimentally.

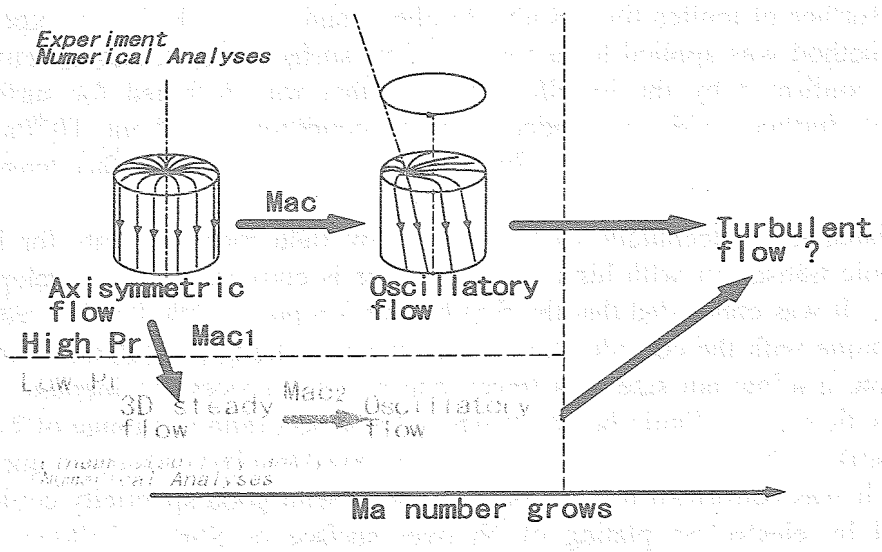

Fig. 1-1 Transition phenomena of thermocapillary flow

Most previously documented experiments have dealt with transparent fluid of a high Pr number in ambient temperature; it is easy to handle such a fluid and to observe its flow field. In contrast, experiments with low Pr number fluids, which are generally molten metals and alloys, have been few. This is due to following reasons:

(1) Low Pr number fluids are opaque. The flow field cannot be observed by means of a visual ray.
(2) Surface of base metals is easily oxidized above its melting point. An oxidation film suppresses thermocapillary flow.
(3) High temperature at which metals are in liquid state makes it difficult to handle.

Figure 1-2 shows the influence of the Prandtl number on the critical Reynolds number obtained by linear stability analysis and direct numerical simulation. In the case of tin with Pr number of 0.01, 5.0mm in height, and unity in aspect ratio, the temperature difference at the first and the second bifurcation point is about 1.6K and 5.3K, respectively. These values are much smaller compared to those for high Pr number materials.

Table 1-1 summarized the previous experiments using low Pr number fluid. It should be noted that most experiments were carried out for a purpose concerning a crystal growth research, that is, the objectives focused on whether oscillatory flow would produce impurity in striation during crystal growth. To date, few observations and measurements of flow and temperature fields have been conducted in low Pr number materials.

Nakamura et al. [1], [2] measured temperature at the free surface by means of thermocouple and flow velocity by tracking some particle movements observed by X-ray in a molten silicon column of 10mm in diameter. Frequency of temperature fluctuation was 0.1Hz at a temperature difference of 100K. However, the imposed temperature difference was far from the second bifurcation point, hence, it is difficult to discuss the transition phenomena of Marangoni flow. Han J., et al. [3] experimentally investigated thermocapillary convection in the liquid bridge of mercury. Free surface fluctuations were measured by non-contacted diagnostic method, and they found the critical Marangoni number, detecting it to be 900 with an oscillatory frequency around 5Hz. However, since they used copper rods to sustain the liquid bridge, a copper-mercury amalgam was formed on the free surface, leading to free surface pollution.

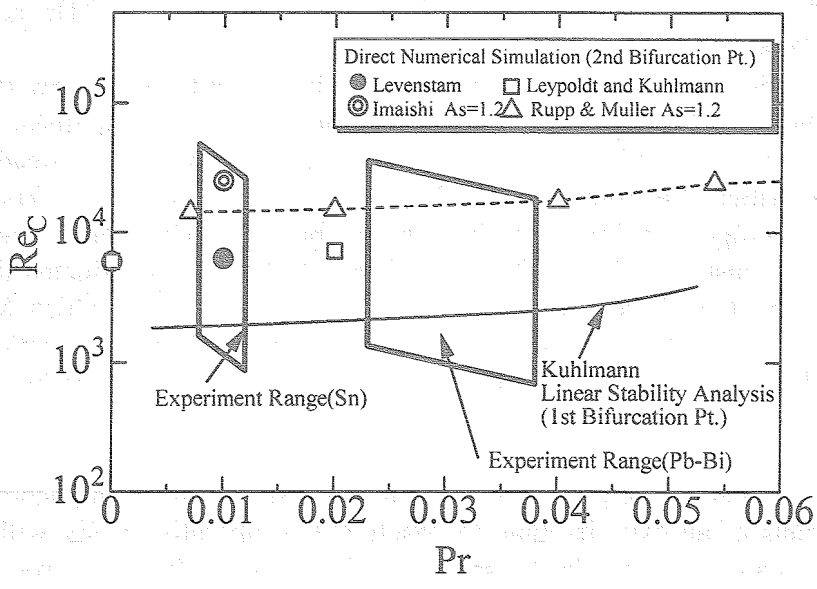

Fig. 1-2 Pr number versus critical Reynolds number in low Prandtl number

Table 1-1 Previous experiments using low Prandtl number fluids

Year	Title	Author	General Description	Paper	Experiment
1983	Experiment on the thermocapillary convection of a mercury liquid bridge in a floating half zone	J.H. Han, W.R. Hu	Liquid bridge of mercury was used. Critical Ma was obtained by detecting surface deformation.	Journal of crystal growth 169(1996)129-135	1g
1989	The Floating-Zone Growth of Ti3Au and Ti3Pt	Y. K. Chang	Ti3Pt crystal was used. Surface striations was observed due to Marangoni convection.	Journal of crystal growth 62(1983)627-632	1g
1990	Floating zone growth of silicon under microgravity in a sounding rocket	A. Eyer, R. Nitsche	Si crystal was used. Surface striations was observed due to Marangoni convection.	Journal of crystal growth 71(1985)173-182	μg
1990	Transition from steady to time-dependent Marangoni convection in partially coated silicon melt zone	A. Croll, R. Nitsche	Si crystal was used. Surface striations was observed due to Marangoni convection. Critical Ma was 100-200.	Proc. VIIth European Symposium on Materials and Fluid Sciences in Microgravity, ESA SP-295	1g, μg
1990	Analysis of periodic non-rotational W striations in Mo single crystals due to nonsteady thermocapilary convection	M. Jurisch, W. Loser	W doped Mo crystal was used. Diameter dependance of critical Ma was obtained.	Journal of crystal growth 102(1990)214-222	1g
1996	Surface temperature oscillations of a floating zone resulting from oscillatory thermocapillary convection	M. Jurisch	Mo and Nb crystal was used. Surface striation and surface temperature fluctuation was measured. The frequencies by both measurements agreed. Electron beam heating facility was used.	Journal of crystal growth 102(1990)223-232	1g
1996	Experimental and numerical studies of thermocapillary convection in a floating zone like configuration	M. Levenstam, M Andersson	Si crystal was used. Temperature fluctuations near free surface was measured. Temperature fluctuation was seen. Numerical calculations were conducted.	Journal of crystal growth 158(1996)224-230	1g
1996	Thermocapillary convection in a low-Pr material under simulated reduced gravity	M. Cheng, S. Kou	Molten Si was used. Temperature fluctuation on free surface was measured by pyrometer. At Ma of 6200; temperature difference of 50K, oscillation 0.07Hz and 4K in amplitude was observed.	Proc. of 4th microgravity fluid physics & transport phenomena conference, 1998	1g
1998	Thermocapillary convection in a low-Pr material under simulated reduced gravity conditions	Y. Tao, S. Kou	Molten tin was used. Temperature fluctuation was measured by T/C. At temperature difference of 85K, oscillation of 5Hz and 1.3K in amplitude was observed.	Proc. of 2nd microgravity fluid physics & transport phenomena conference, 1998	1g
1998	Temperature fluctuations of the Marangoni flow in a liquid bridge of molten silicon under microgravity on board the TR-IA-4 rocket	S. Nakamura, T. Hibiya	Molten Si was used. Temperature fluctuation near free surface was measured by T/C. At melting process, 0.1Hz of temp. fluctuation was observed. In 1g, 0.2Hz was obtained.	Journal of Crystal Growth 186(1998) 85-94	1g, μg

Mukai et al. [4] presented changes in surface tensions (σ) and its temperature coefficient (σ_T) of molten silicon with changing ambient oxygen partial pressures. The values of σ and σ_T were strongly dependent on the oxygen partial pressures ranging from 10^{-25} to 10^{-14}MPa and, hence, it is predicted that Marangoni flow will be affected by the partial pressure and oxygen concentration in the melt [2]. Since the reactivity of molten tin, which is a present test fluid of our experimental study, toward oxygen is similar to that of molten silicon, actual values of σ and σ_T in our experiment chamber will be required.

Kou S., et al. [5] measured temperature fluctuation on the free surface in molten silicon of 13mm in diameter by pyrometer. According to their measurement, a frequency of 0.07Hz and amplitude of 4K were obtained at Marangoni number of 6200. According to the numerical calculations by Imaishi et al. [6], frequency of surface temperature fluctuation is in the order of 10^{-1}Hz even for much lower Marangoni numbers: 0.31Hz accompanies Ma number of 226 (Pr=0.01, As=1.2, a=6.5mm).

Various theoretical and numerical analyses have been conducted in low Pr number fluid. Kuhlmann [7] and Chen [8] investigated transition phenomena by using linear stability theory. They showed that thermocapillary flow transitioned from axisymmetric steady to 3D steady flow beyond the critical Reynolds number, Re_{cr}, and investigated the influence of the aspect ratio of the liquid bridge, heat loss from free surface, buoyancy convection, and so on. Rupp and Muller [9], Levenstam [10], Kuhlmann [11], and Imaishi [6] conducted direct numerical analyses, and found that there was the second bifurcation point at which Marangoni flow transitioned from 3D steady to 3D oscillatory in addition to the first one mentioned above.

In a word, the critical Marangoni number has been rarely determined by an experimental approach in low Pr number fluid successfully.

The overall purpose of the present study is to understand transition phenomena in molten materials by means of an experimental approach and comparative study with the numerical works in this research group. In Japanese fiscal year of 1998, we have carried out the preliminary works which have mainly comprised selection of the fluid (*i.e.* molten tin) and the sustaining material for the liquid bridge (*i.e.* iron), preparation of the experimental devices,

and measurements of surface temperature fluctuation of molten tin. These are described in the previous issue in detail [12]. However, reproducibility of the surface temperature fluctuations obtained was insufficient. This is mainly due to low sensitivity of the installed measurement system of surface temperature and surface oxidation of molten tin during an experiment.

In 1999, measurement technique of surface temperature has been developed and the new technique has made it possible to observe surface temperature fluctuations of molten tin successfully near the second bifurcation point. Consideration concerning surface science of tin has led us to design of unique experiment apparatus where clean surface of molten tin has been able to obtain and sustain during an experiment. The new chamber has been constructed with co-operative works by Sukegawa Electric Co. Ltd., and performances of the chamber have been already confirmed. Novel visualization technique of flow field measurements for molten tin using ultrasonic transducer with high heat resistance is currently under development by consignment works to Toshiba Co. We can conclude that the first bifurcation point will be detected by this technique from the experimentally predicted performances such as a resolution, a minimum size of a tracer, and a signal processing method by the consignment works. The visualization technique requires development of unique balloon-like tracer also. The development is carrying out by collaboration with Kagoshima Prefectural Institute of Industrial Technology, in which the tasks for NASDA partly consign to NTT Advanced Technology Co. The surface tensions of molten tin in the experiment chamber have been studied by *in site* measurements. This study is carrying out by collaboration with Kyushu Institute of Technology and will lead to understanding the oxygen partial pressure dependency of σ and σ_T of molten tin.

Many works have been done in this year, and we will be able to prove the flow transition from 3D steady to oscillatory in low Pr number fluid in the near future.

2. TEMPERATURE FLUCTUATION MEASUREMENT

2-1. Reinvestigation of Measurement Instrument for Surface Temperature

A measurement result of surface temperature oscillation observed by thermviewer has been reported in the previous report [12]. Some experiments under same conditions were repeated in order to confirm the reproducibility of the observed result after that. However, no definite temperature oscillation was observed. Except for quenching oscillatory thermocapillary flow by surface contamination, one of the reasons for not observing temperature oscillation is insufficient performances of the thermviewer for detecting radiation from cylindrical surface with very low emissivity. In addition to this reason, precise temperature difference of the liquid bridge (Marangoni number) corresponding to data measured by the thermviewer was unknown because recorded data was not synchronized to temperature data of the rods. This means important information such as temperature difference of the liquid bridge, at which oscillations have begun, and correlation between the temperature difference and oscillating motion lacks.

Selection of radiation thermometer was investigated again and made correction by applying Japan Industrial Standard for radiation thermometer.

Selection of Radiation Thermometer

Radiation energy at a constant emissivity is expressed theoretically with the following Planck equation [13]:

$$E(\lambda,T) = \varepsilon(\lambda,T)c_1 n^{-2}\lambda^{-5} / \{\exp(c_2/\lambda T) - 1\} \qquad (3\text{-}1)$$

E	$W/(m^2 \cdot \mu m)$	: Radiation energy
ε		: Emissivity
$c_1 = 2\pi h c_0^{\,2}$	$W \cdot \mu m^4 / m^2$	
$h = 6.6256\times10^{-34}$ J·s		: Planck constant
$c_0 = 2.997925\times10^{8}$ m/s		: Light velocity
n		: Refractive index (n=1, in vacuum)
$c_2 = hc_0/k = 1.43879\times10^{4}$	$\mu m \cdot K$	
$k = 1.38054\times10^{-23}$ J /K		: Boltzmann constant

Figure 2-1 shows the detectable range of wavelength by four kinds of photo detectors (Si, InGaAs, PbS, and HgCdTe) plotted on radiation curves of Sn calculated by above equation (Assumed emissivity: 0.04, constant). The red line, blue line and green line show the radiation curves of Sn at 773.15K, 723.15K, and 673.15K, respectively. This temperature range from 673.15K to 773.15K is typical experimental range in the low Pr study. The PbS and HgCdTe photo detectors can detect in higher radiation energy than other Si and InGaAs photo detectors relatively. Actually, theoretical radiation energy is reduced to some extents at a measuring port by absorption. The dotted line in wavelength range of PbS and HgCdTe shows such reduction caused by appropriate optical pass filter. Comparisons of detectable radiation energy (center of wavelength range) which can detect by above four kinds of photo detectors are shown in Fig. 2-2. It is concluded that PbS photo detector can detect proper wavelength range with high radiation energy for the low Pr experiment.

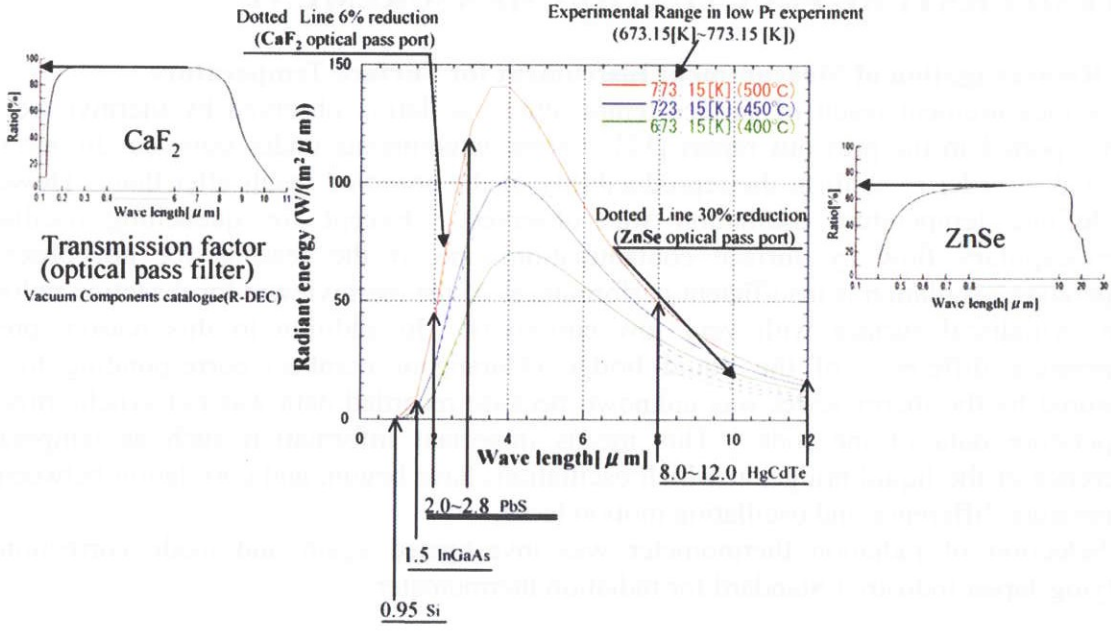

Fig. 2-1 Estimation of radiation energy
detectable by available pyrometers

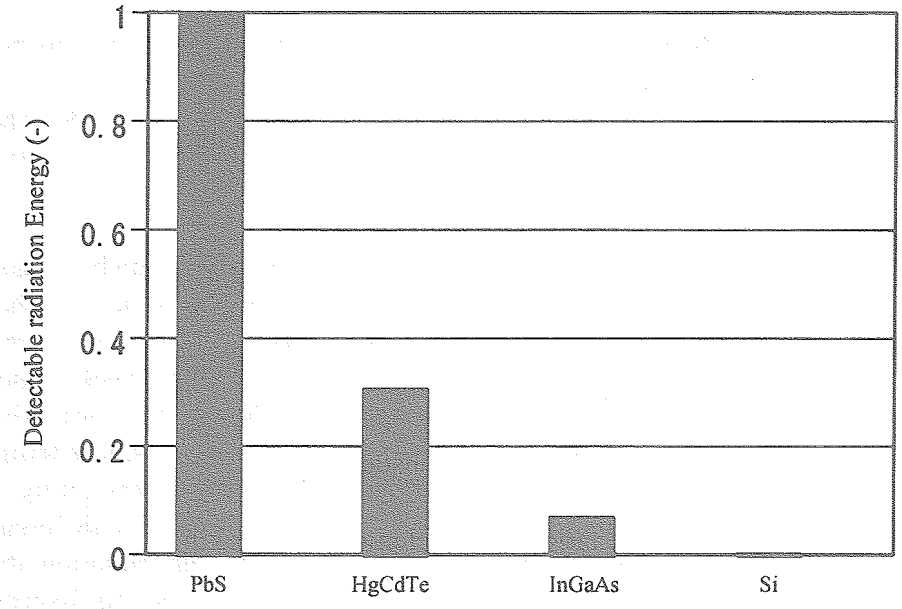

Fig. 2-2 Detectable radiation energy (normalized) under 723.15[K] & center of wavelength range

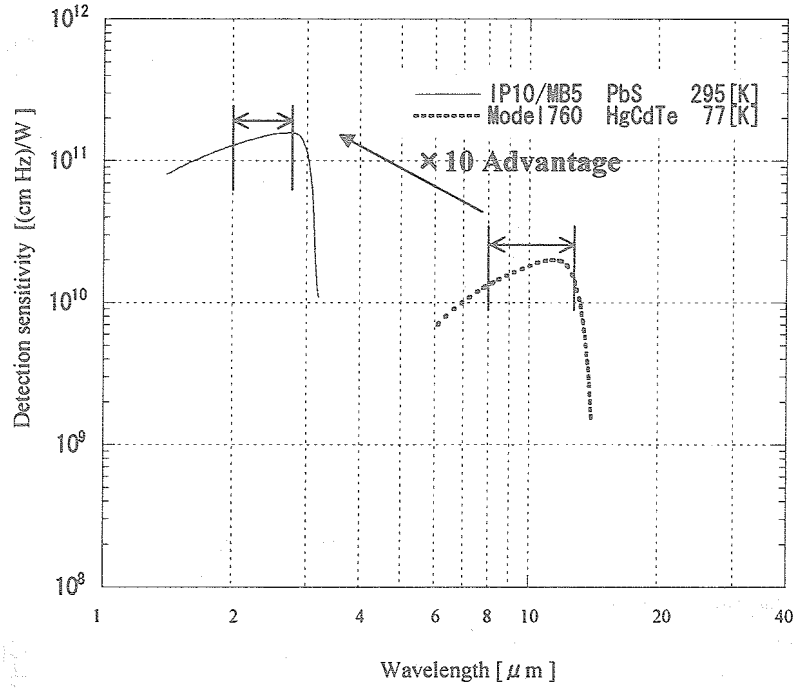

Fig. 2-3 Detection sensitivity of photo detectors (PbS & HgCdTe)

In addition to above investigation, it is necessary to investigate the detection sensitivity of photo detectors for measuring data with fine signal to noise ratio. Figure 2-3 shows the detection sensitivity characteristics of PbS photo detector plotted with that of HgCdTe photo detector for comparison. The PbS photo detector has sensitivity approximately ten times higher than that of the HgCdTe if the same radiation energy is received by them [14]. Theoretically, the PbS photo detector can receive radiation energy two times higher than that

of the HgCdTe (Fig. 2-1), hence, surface temperature data with fine signal to noise ratio is expected by using the PbS detector.

It should be concluded, from investigation above, that PbS photo detector (IMPAC Electronic GmbH, IP10/MB5) is optimum measuring instrument in the low Pr experiment.

Performance Test of Radiation Thermometer

To measure surface temperature by a radiation thermometer is much advantage not to disturb the flow field of the fluid. In particular, it is effective measurement method for small measuring object such as the liquid bridge in the low Pr experiment. However, measuring performance shown on operation manual of radiation thermometer can easily change because output signal is affected sensitively on atmosphere between detector and measuring object or surface conditions of the object. In the low Pr experiment, not the absolute temperature but relative fluctuation component is necessary. The performance for investigating temperature resolution under same measuring conditions was tested in order to validate the measured data.

Figure 2-4 shows the experimental arrangement for testing the radiation thermometer, which is defined by Japan Industrial Standard: JIS C1612 (general rules for expression of the performance of radiation thermometers). The fixed-point blackbody furnace of Zn was used as measuring object that can keep at the constant temperature for several minutes. The constant temperature, 692.73K, is very close to temperature level in the low Pr experiment. Measurement system using in the low Pr experiment was also used and set quite same sampling interval as practical experiment. Change of output signal level was measured by inserting the reflector to optical path (blackbody - photo detector) in order to cut the radiation input.

Result is shown in Fig. 2-5. Resolution of radiation thermometer is identified as 0.24K by statistical analysis of measured data. The frequency characteristic was also investigated by FFT analysis and identified as governed by white noise (no significant frequency characteristic).

It is concluded that this radiation thermometer has temperature resolution that is smaller than amplitude of temperature fluctuation at oscillatory thermocapillary flow.

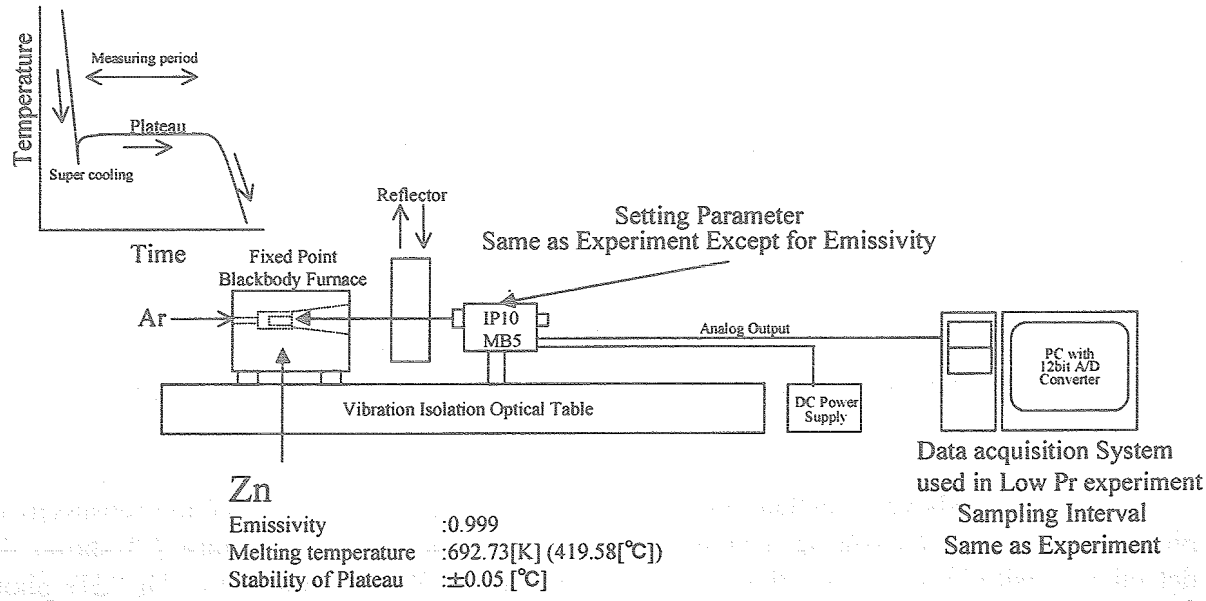

Fig. 2-4 Experimental arrangement for testing the radiation thermometer

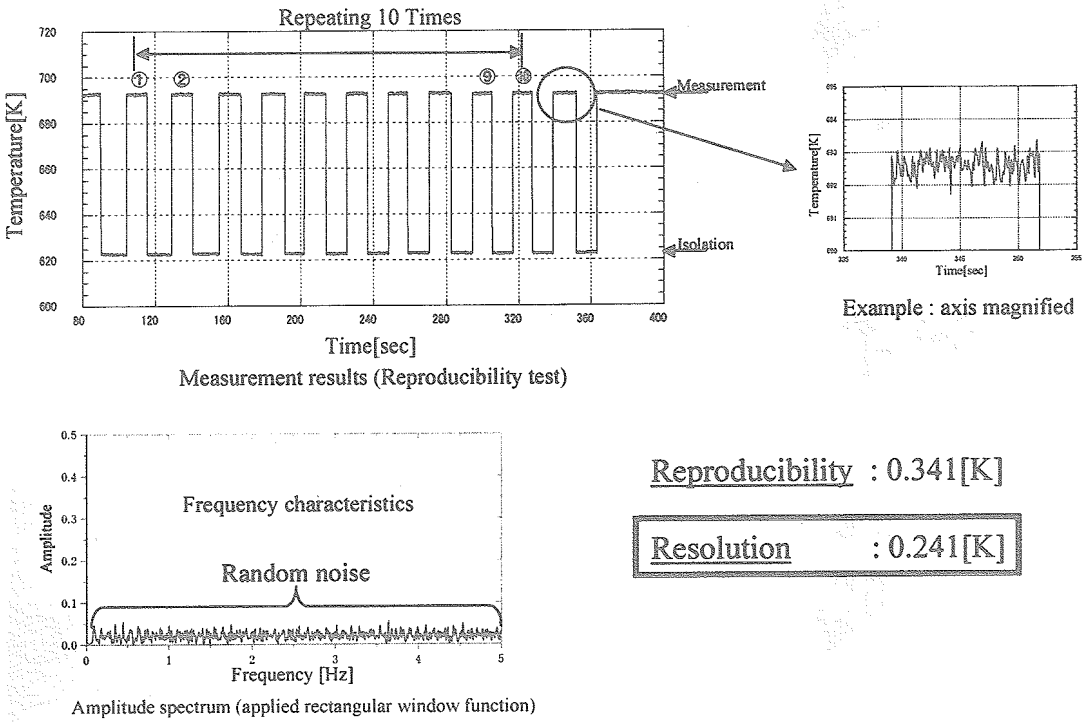

Fig. 2-5 Performance test results of IMPAC IP10/MB5

2-2. Measurement of Surface Temperature Oscillation

The present object taking in this experimental term is to confirm the definite oscillatory thermocapillary flow by measuring surface temperature fluctuation of the liquid bridge. The diameter of the liquid bridge tested in previous experimental term to validate the reproducibility is 10mm. However, selected diameter of the liquid bridge tested in this term is 3mm so that the enough temperature difference as driving force should be imposed for thermocapillary flow.

Experimental Conditions

An experimental apparatus is illustrated in Fig. 2-6 [12], in which an optical pass filter made of CaF_2 has not been installed. This figure also shows the attached radiation thermometer and image of measuring area on the liquid bridge surface (2.2mm in diameter). Figure 2-7 shows a CCD image of the liquid bridge between a pair of upper and lower rods formed in a vacuum condition (approximately 5×10^{-2} [Pa]). The temperature difference was imposed by heating the upper rod at a constant power and cooling the lower rod naturally. A time series of temperature of the upper and the lower rods measured by thermocouples embedded at near the end face of them and imposed temperature difference (maximum 22.0[K]) are shown in Fig. 2-8 and 2-9, respectively. The rate of heating is approximately 2.6×10^{-2} [K/sec].

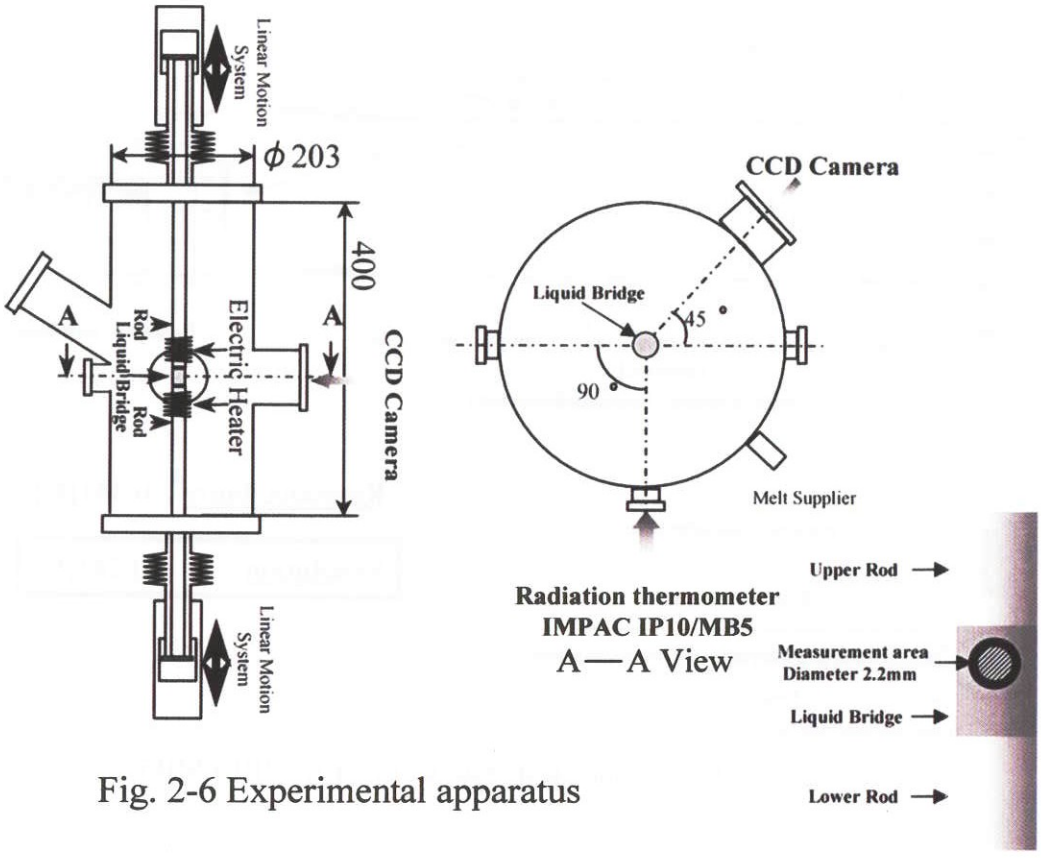

Fig. 2-6 Experimental apparatus

CCD image of liquid bridge

Diameter	: 3.0 [mm]
Height	: 3.35 [mm]
Aspect ratio(height/radius)	: 2.23
Vacuum condition	: 5×10^{-2} [Pa]
Sampling interval (Data acquisition system)	:10[Hz]

Fig. 2-7 CCD image of the liquid bridge

Results and Discussion

Figure 2-10 shows the time series of surface temperature measured by the radiation thermometer, indicating existence of standing wave in the time of 200-300sec with very small amplitude but with distinguishable one (its amplitude is larger than temperature resolution of the radiation thermometer). The fluctuating component was extracted by shifting baseline, as shown in Fig. 2-10 and 2-11, in order to observe the growth of the standing wave. The periodic fluctuation begun after 200sec and amplitude of the fluctuation became slightly larger than before. This periodic fluctuation continued approximately 100sec, then damped gradually. The temperature difference of this onset of the periodic fluctuation was 7.6K, which was near the second bifurcation point (see Section 2-3). The amplitude spectrum of each sampling time of 100sec at 50sec intervals was obtained by FFT analysis as shown in Fig. 2-12. It is clear that the characteristic frequency near 0.17Hz rose after 200-300sec, and the frequency shifted toward slightly higher value as temperature difference increased.

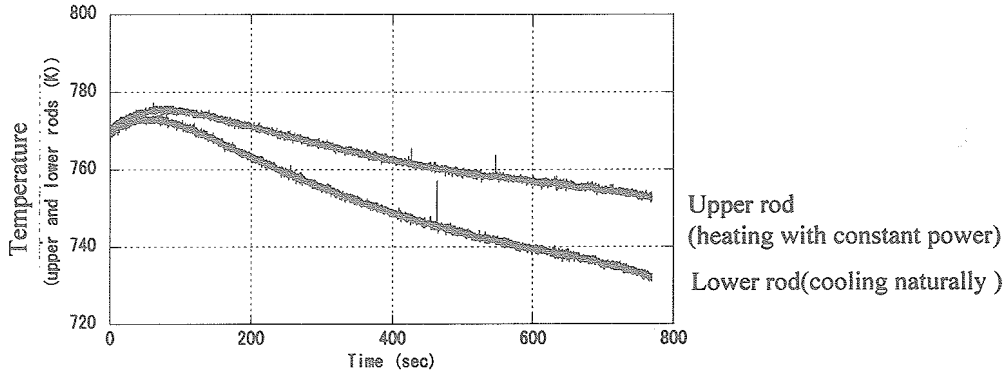

Fig. 2-8 Temperature of upper and lower rods

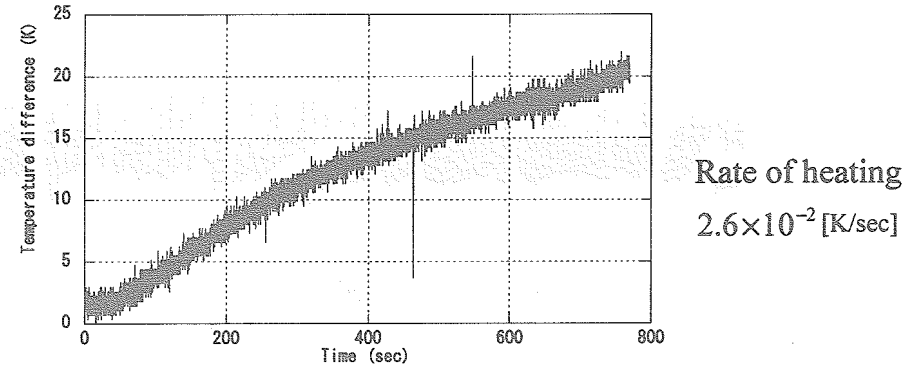

Fig. 2-9 Imposed temperature difference

The damping of amplitude is considered as a result of reduction of temperature coefficient of surface tension caused by oxidation of fluid surface. The extremely thin oxidation film covered with whole liquid bridge surface was observed by CCD image at the end of experiment. The standing wave measured with 0.17Hz can be considered as a result of a pulsating or/and rotating oscillation, however, to conjecture and clarify this oscillating motion is impossible from only one-point measured data. The oscillating motion of pulsating or rotating will be made clear near the future by multi-point measuring.

Numerical simulation under conditions just same as this experiment was performed and reported in Section 2-3. It should be noted that Prof. Imaishi and Dr. Yasuhiro are studying the transition behaviors of low Pr number fluids for general understanding, while we are carrying out the simulations for interpretation of experimental results.

The experiment under different conditions was performed at same procedure. These results are summarized in Table 2-1.

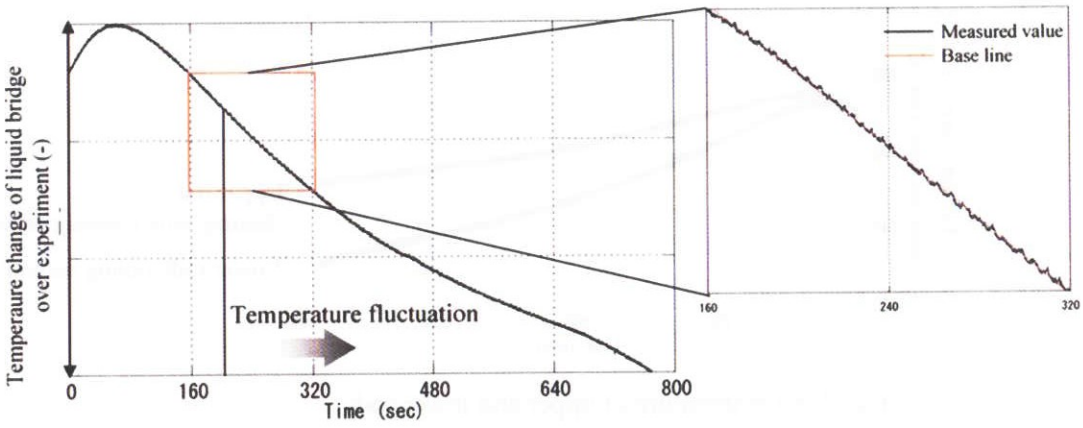

Fig. 2-10 Temperature fluctuation measured by radiation thermometer

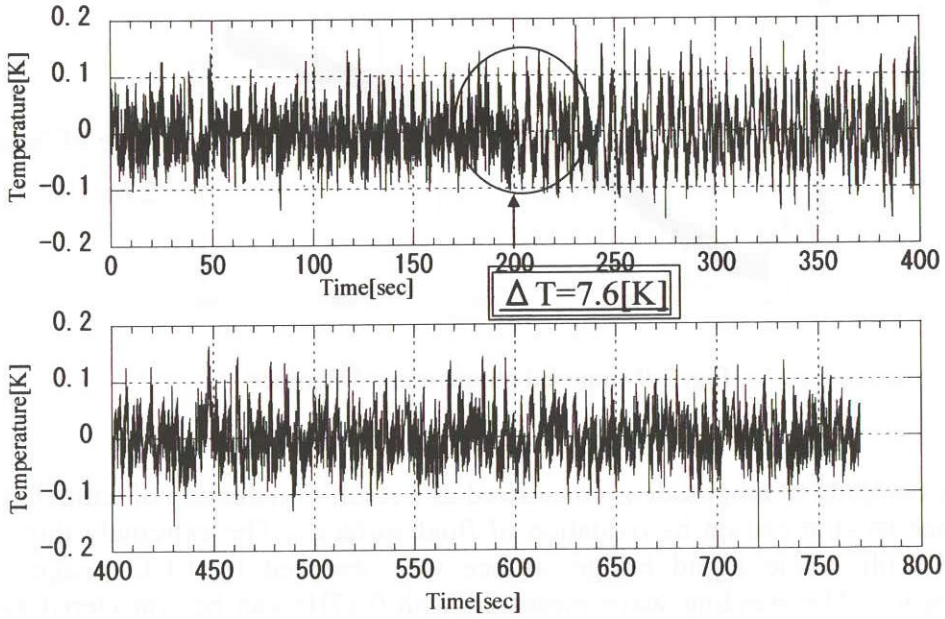

Fig. 2-11 Extracted temperature fluctuation component

Periodic temperature fluctuation of the liquid bridge surface, which have been measured near the second bifurcation point, and correlation between frequency shift of the oscillation and the temperature difference have been never reported before in experimental works [1], [5], [15]. In this study, we successfully measured them by using the optimum radiation thermometer of which performances was predicted theoretically and confirmed experimentally. More precise results of temperature fluctuation will be obtained by the promising technique of surface temperature measurement mentioned above in conjunction with using a new experimental chamber where clean surface of molten tin will be obtained and sustained during an experiment (see Section 3). The parametric study changing diameter and aspect ratio of the liquid bridge with multi-point surface temperature measurement will be performed later. The experiment for measuring practical oxidation effect which reduce surface tension and its temperature dependency (used in calculating Marangoni number) as the driving force for thermocapillary flow has just begun. This is reported in Section 2-4.

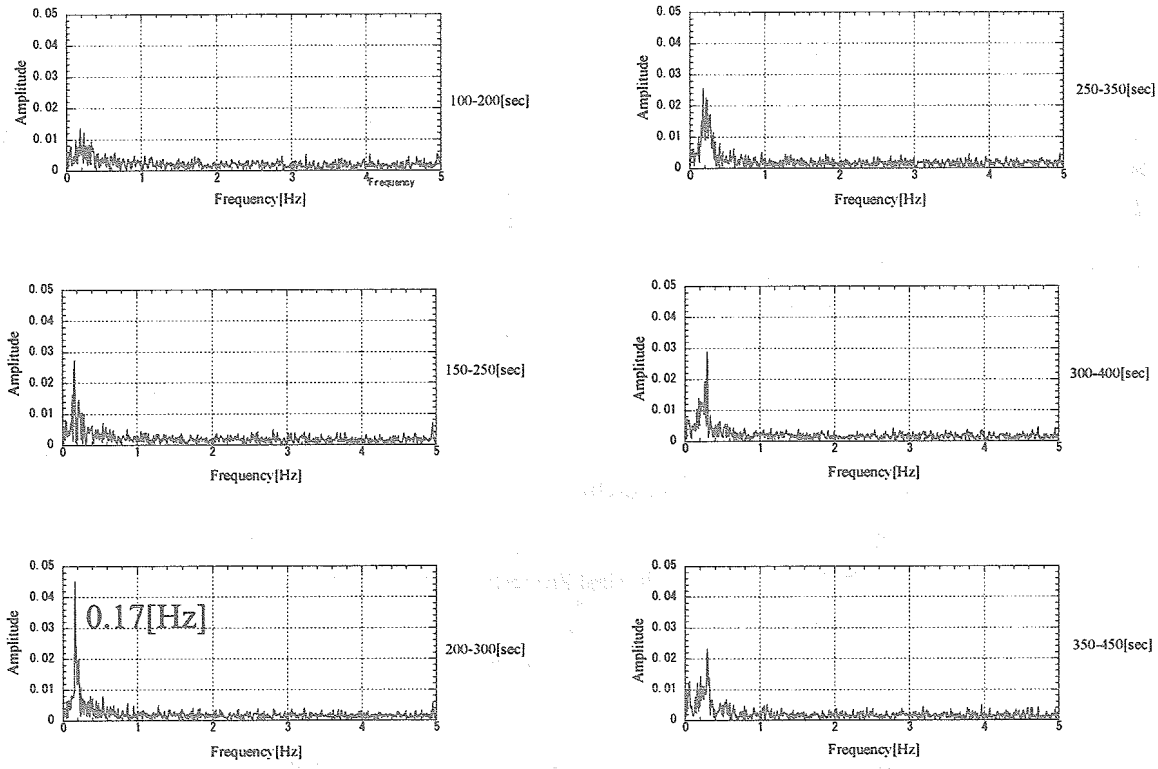

Fig. 2-12 FFT analysis of measured temperature fluctuation

Table 2-1 Experimental Results

Case	1	2
As (-)	2.23	2.5
ΔT (K)	7.6	12.75
f (Hz)	0.17	0.2, 0.3
ω (-)	0.115	0.135,0.20

$\omega=2\pi a^2 f/\alpha$

2-3. Numerical Simulations

Numerical simulation under conditions just same as experiment was conducted. Purpose of present simulations was to check onset point obtained by the experiment. The simulation program was developed by Professor Imaishi and Dr. Yasuhiro. It was modified by Dr. Yasuhiro so that we could deal with transit thermal boundary conditions and dimensional data convenient for comparison with experimental data directly. A size of the liquid bridge to be analyzed was specified the typical experiment case, in which radius a=1.5mm and height h=3.35mm was employed, thus aspect ratio As=2.23, as shown in Fig. 2-7. Figure 2-13-1 shows fitting functions of temperature changes of the hot and cold iron walls imposed in the experiment. They were built in the program as thermal boundary conditions. Temperature difference ΔT as shown in Fig. 2-13-2 was induced by difference of cooling rates of the irons. Thermophysical properties of melted tin were used as shown in Table 2-2. All values except surface tension derivative were interpolation values at arithmetic mean temperature 753K of maximum temperature at the hot wall and minimum one at the cold wall during the experiment.

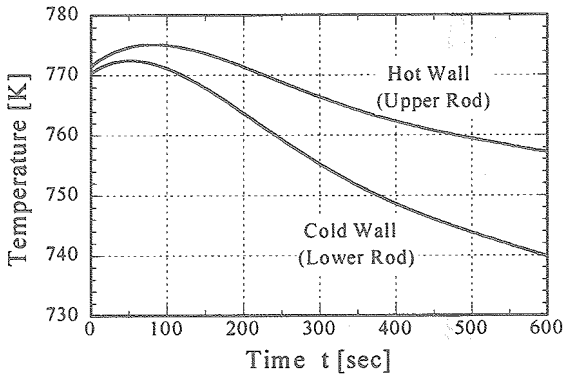

Fig. 2-13-1 Temperature changes of the iron walls

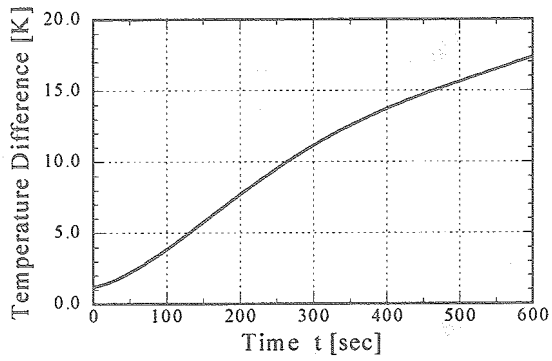

Fig. 2-13-2 Temperature difference

Table 2-2 Thermophysical Properties of Melted Tin at 753 [K]

Viscosity	$\mu = 1.1856 \times 10^{-3}$	[Pas]
Density	$\rho = 6.793 \times 10^{3}$	[kg/m3]
Thermal Conductivity	$\lambda = 3.5437 \times 10^{1}$	[W/mk]
Heat Capacity	$Cp = 2.42 \times 10^{2}$	[J/kgK]
Surface Tension Derivative	$\sigma_T = 1.3 \times 10^{-4}$	[N/m/K]
Prandlt Number	$Pr = 0.008$	

According to the experimental result, onset of temperature fluctuation was observed at t=198sec (ΔT=7.6K). In order to confirm temperature fluctuation in simulation, start time of this calculation was set t=350sec (ΔT=12.7K) when enough time had past after onset point obtained by the experiment. Figure 2-14-1 and 2-14-2 show temperature changes of the walls and the temperature difference, respectively. Calculated surface temperature and velocity components at local point of middle height of the liquid bridge are shown in Fig. 2-15-1 and 2-15-2, respectively. Fluctuation of temperature was observed at t=352sec after quick decrease. The data of temperature and velocities contained a lot of frequency components comparing to the results of analysis with lower aspect ratio As=1.8 conducted by Professor Imaishi et al. [16]. FFT analysis of the surface temperature revealed temperature fluctuation had two components of f=0.6 and 1.0Hz as shown in Fig 2-15-3. They were larger than value f=0.17Hz obtained by the experiment (Fig. 2-12). The difference could be due to large ΔT imposed at start time rather than difference in aspect ratio.

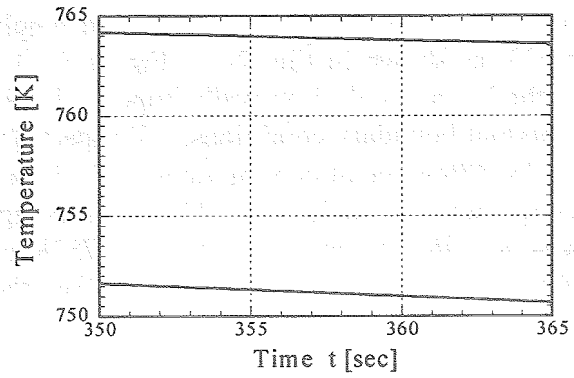

Fig. 2-14-1 Temperature changes of the iron walls

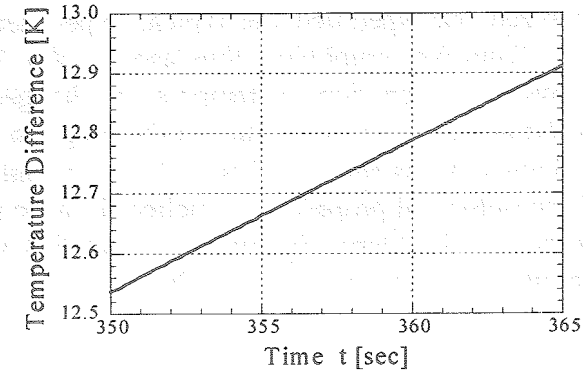

Fig. 2-14-2 Temperature difference

It was considered that state of fluctuation was different whether calculation started before onset point or not. We estimated onset point in numerical simulation in order to start calculation before fluctuation, showing considerable calculation time to investigate time interval containing onset point obtained by the experiment. Therefore following method was adopted: changes of boundary temperatures were accelerated 10 times of the actual changes as shown in Fig. 2-16-1 and 2-16-2, hence start time was set t=180.0sec (ΔT=6.9K). By using such conditions, calculation time was saved for wide range of ΔT=6.9 to 12.0K. Figure 2-17-1 and 2-17-2 shows fluctuations of surface temperature and velocities, respectively. It was considered onset point existed at t=181.4sec (ΔT=7.4K). As a result of this analysis, onset point was almost same as the experimental result although changing rates of the boundary temperatures were accelerated. Onset point of t=180.0+10(180.0-181.4)=194.0sec was estimated in actual changes of the boundary temperatures.

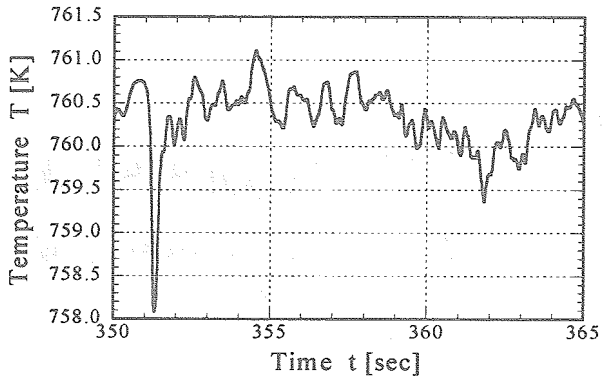

Fig. 2-15-1 Fluctuation of surface temperature

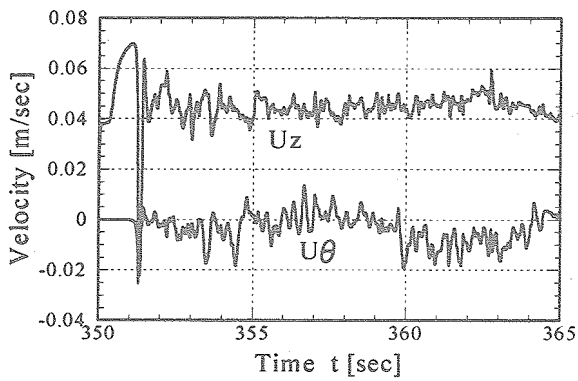

Fig. 2-15-2 Fluctuations of surface velocities

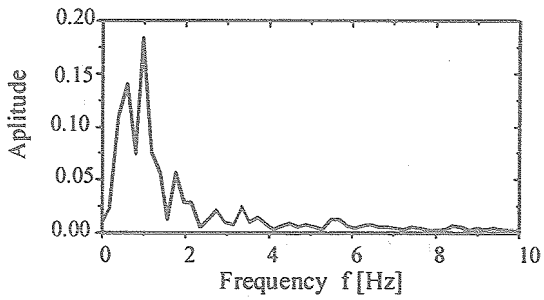

Fig. 2-15-3 FFT analysis of temperature fluctuation

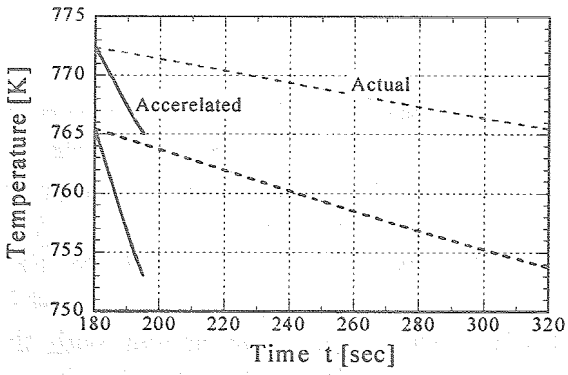

Fig. 2-16-1 Accelerated temperature changes of the iron walls

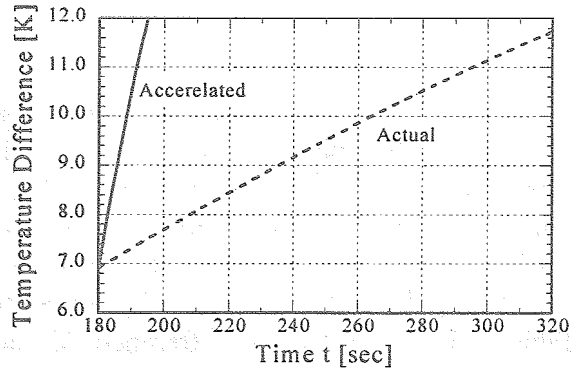

Fig. 2-16-2 Temperature difference

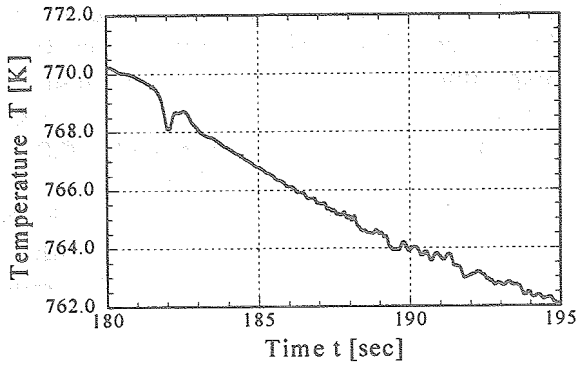

Fig. 2-17-1 Fluctuation of surface temperature

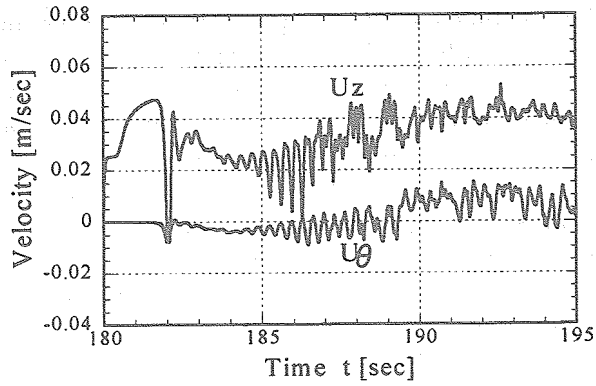

Fig. 2-17-2 Fluctuations of surface velocities

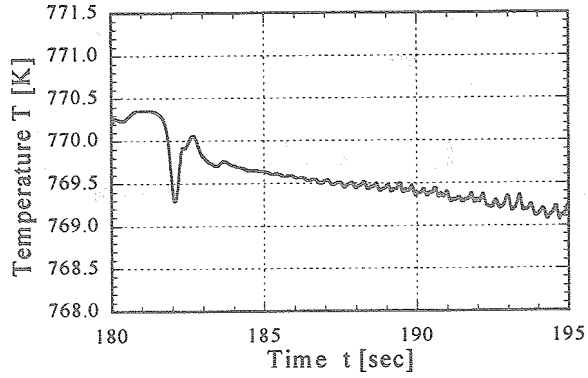

Fig. 2-18-1 Fluctuation of surface temperature

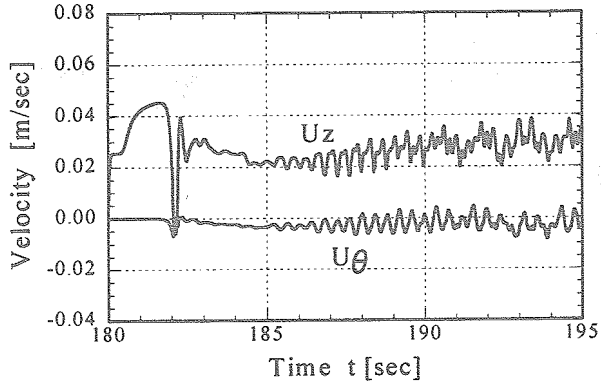

Fig. 2-18-2 Fluctuations of surface velocities

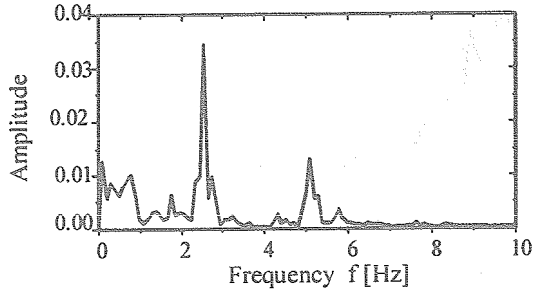

Fig. 2-18-3 FFT analysis of tempereture fluctuation

A simulation was conducted again in the actual boundary conditions to obtain surface temperature fluctuation data. Figure 2-18-1 shows fluctuation of surface temperature. Onset point was observed near at t=185.0sec (ΔT=7.1K). As same as the temperature, fluctuations of velocity components on free surface grew at same time as shown in Fig. 2-18-2. As shown in Fig. 2-18-3, a peak of amplitude was appeared at f=2.6Hz by FFT analysis. The results obtained by the simulation and the experiment were summarized in Table 2-3. Temperature difference ΔT at onset point was in good agreement with the experimental result, however, frequency f was estimated 15 times larger than the experiment. Difference in f will be investigated by Professor Imaishi et al. and us as future work. As a result of a series of simulations, we obtained knowledge that state of temperature fluctuation

is different by an initial ΔT and a heating rate imposed to a specimen. It should be considered in planing of experimental conditions and analysis of a result.

Table 2-3 Comparison Result of Simulation with Experimental Result
<Pr=0.08,As=2.235>

	Simulation	Experimet
Temperature Difference at onset ΔT[K]	7.1	7.6
Frequency f[Hz]	2.6	0.17

2-4. *In Situ* Measurement of Surface Tension

Mukai et al. [4] presented changes in surface tensions (σ) and its temperature coefficient (σ_T) of molten silicon with changing ambient oxygen partial pressures. The values of σ and σ_T were strongly dependent on the oxygen partial pressures ranging from 10^{-25} to 10^{-14}MPa. Since driving force of Marangoni convection is surface tension gradient along free surface of a fluid and the reactivity of molten tin toward oxygen is similar to that of molten silicon, actual values of σ and σ_T in our experiment chamber should be measured. Moreover, such values will be useful for verifying performances of a new experiment chamber (see Section 3-3). In this year, experimental setup and preliminary measurements were carried out with the new chamber for the low Pr experiment (see Fig. 3-3) and an apparatus of Kyushu Institute of Technology (KIT). Research procedure, the apparatus, and the method are given in this report. Only one figure was presented in Section 3-3 (Fig. 3-6), details of the results will be published in the next issue.

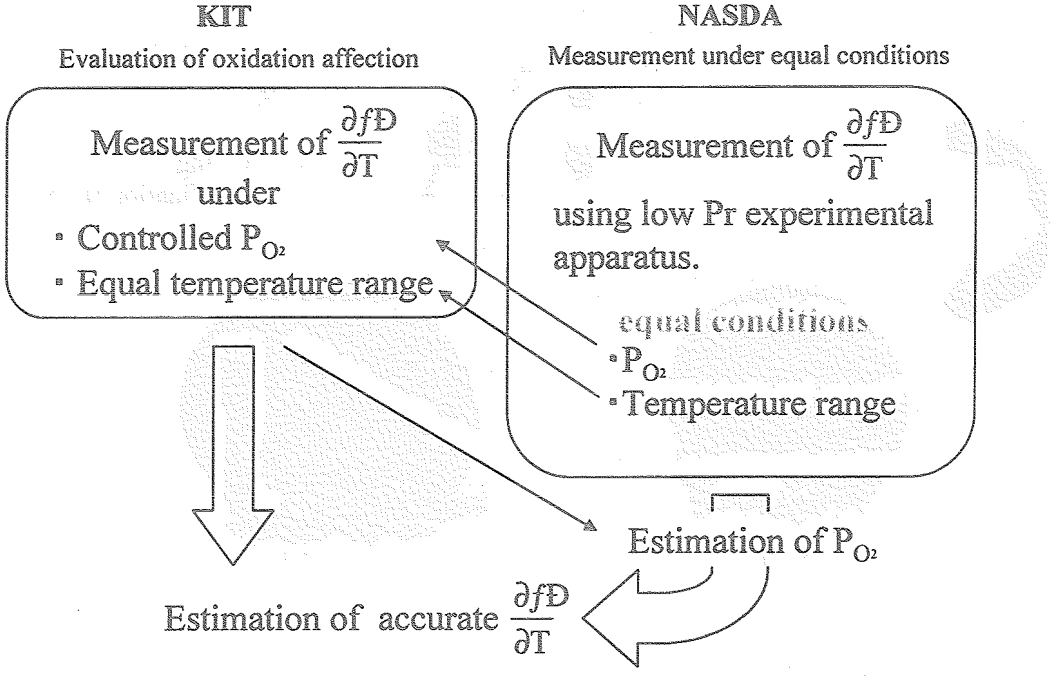

Fig. 2-19 Research procedure of surface tension by *in situ* measurement

Most important information is actual values of σ and σ_T of molten tin during a low Pr experiment; hence surface tensions should be measured *in situ*. Since it is difficult to measure oxygen partial pressure (P_{O2}) in a vacuum chamber precisely, we can obtain the surface tensions at a certain P_{O2} (x Pa) and given temperatures (T_n K) by *in site* measurements. The unknown partial pressure of x Pa can estimate by measurements of surface tensions at carefully controlled P_{O2} and the given temperatures of T_n K by using the apparatus where P_{O2} can control below 10^{-22}MPa under Ar gas flow at the total pressure of 0.1MPa [17]. And then, systematic measurements using the above apparatus can obtain actual values of σ and σ_T at any P_{O2} and temperatures, and will lead to systematic understanding of surface tension behavior in the group VI molten metals. Figure 2-19 shows research procedure mentioned above.

Figure 2-20 shows the experimental setup for *in situ* measurement. Tin droplet of 5mm in diameter was formed on α-Al_2O_3 substrate, of which diameter and thickness was 28 and 4mm, respectively, mounted on the heater unit of the lower disk for sustaining the liquid bridge. The droplet temperature was measured by a thermocouple embedded at near surface of the substrate. Surface tension values were obtained by improved sessile drop method [4], [17]. Analysis methods were the same as the methods for measurement of molten silicon, however, measurement conditions such as employed temperatures and atmosphere, use of a light source, and a size of the droplet and steel ball as a reference were optimized for measurement of molten tin. The apparatus of KIT is shown in Fig. 2-21, where some modifications of the apparatus were carried out for use of an electric heater and a light source. α-Al_2O_3 substrate and grade of reagent tin were just same as the materials used for the *in situ* measurements.

Preliminary results by the *in situ* measurements are described in Section 3-3, where effectiveness of Ar^+ ion etching method for surface cleaning of tin is successfully presented by changes of surface tensions. In next year, detail experiments will be performed for obtaining actual values of σ and σ_T at any P_{O2} and temperatures in the low Pr experiment chamber. Influence of contamination of molten tin by iron, which is a raw material sustained the liquid bridge, on σ and σ_T will be also investigated by using a substrate of which a part of surface is filled by iron.

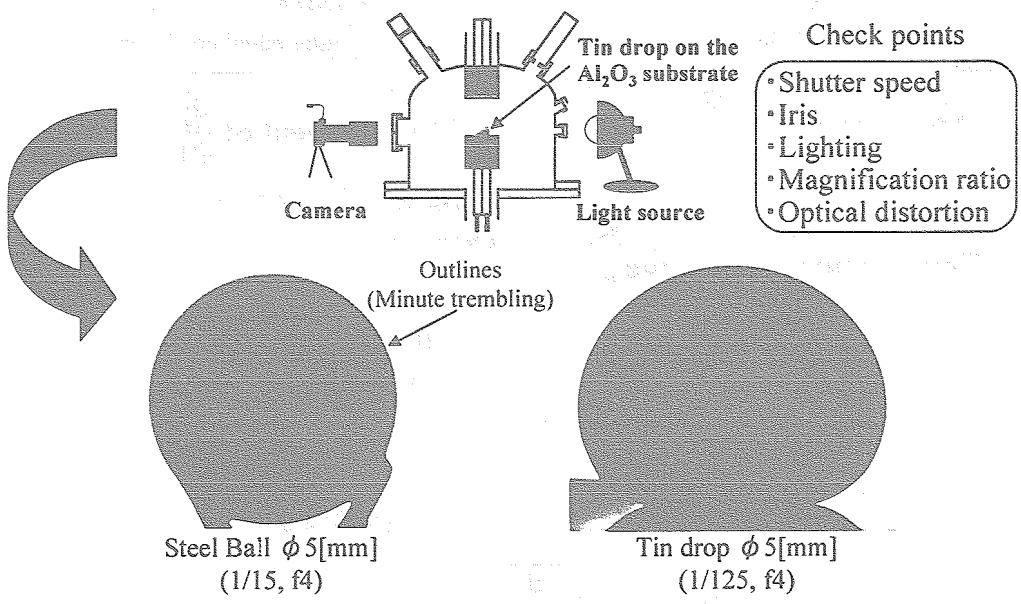

Fig. 2-20 Experimental setup for *in situ* measurement

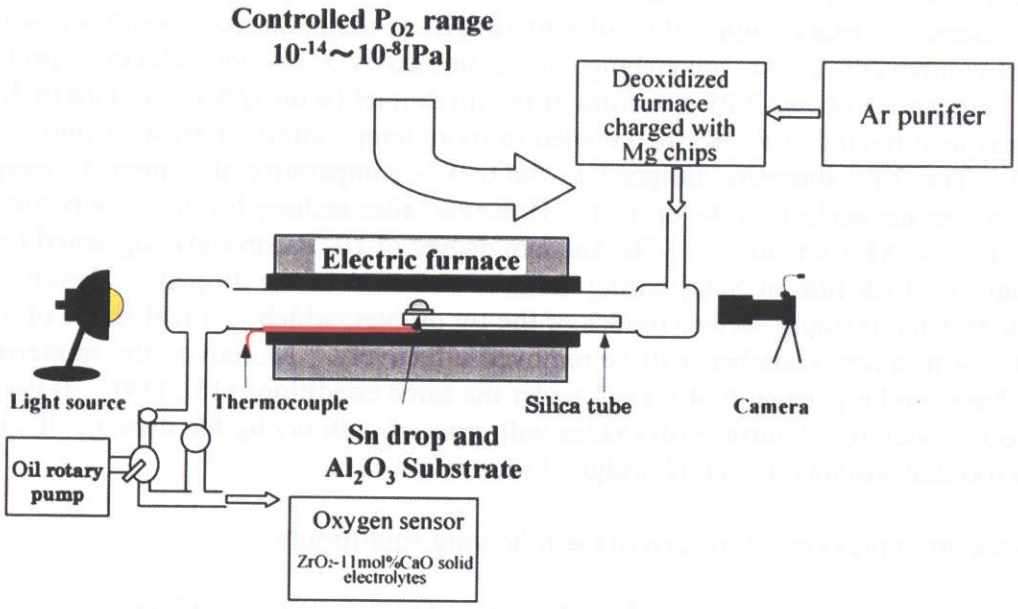

Fig. 2-21 Apparatus controllable P_{O2} below 10^{-22}MPa

3. PERFORMANCES OF NEW EXPERIMENT CHAMBER

3-1. Surface Scientific Considerations of Molten Tin

Since driving force of Marangoni convection is surface tension gradient along free surface of a fluid, it is very important to produce a clean surface and maintain it through a course of an experiment. This means necessity of technique for removal of oxides from a crude fluid and prevention of further oxidation in an experimental study with low Pr number fluids. A throat-capillary method, by which oxides was stripped out at a capillary portion as described earlier [12], was effective for removal of bulk oxides in molten tin. However, there was small amount of residual surface oxides only by the throat-capillary method, and free surface was being covered with oxide film of tin during a course of an experiment at a vacuum degree of 10^{-3}Pa, resulting in insufficient reproducibility of the results [12].

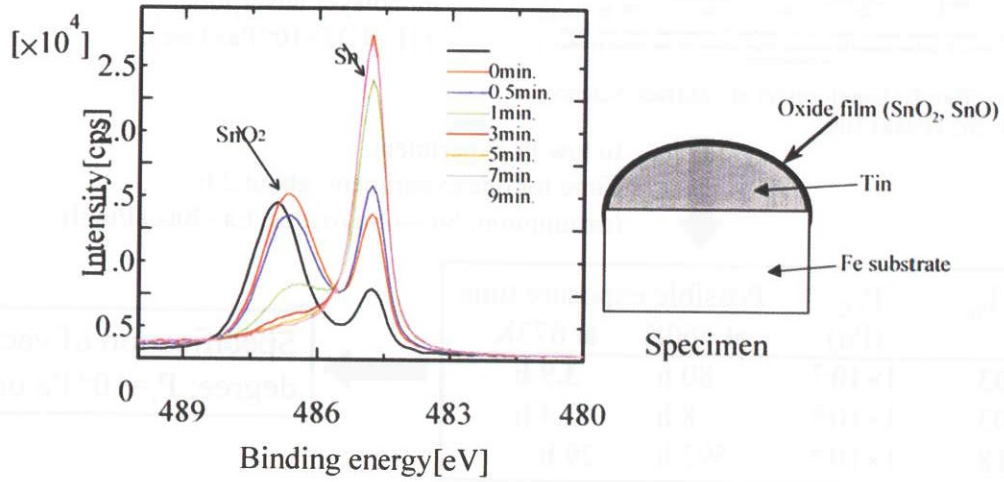

Fig.3-1 XPS spectra on the droplet surface of tin (4mm in diameter)
Each spectrum was obtained after Ar^+ ion sputtering.

Effectiveness of Ar^+ ion etching method has been investigated for removal of the residual surface oxides. Surface composition of a tin droplet in the solid state, combined with depth profile of components by Ar^+ ion etching, was examined by X-ray photoelectron spectroscopy (XPS). Figure 3-1 shows XPS spectrum of the tin droplet (semi-sphere of 4mm in diameter) which was heat-treated at 673K, then cooled to room temperature, under a vacuum condition (10^{-2}Pa). The XPS intensity assigned to SnO_2 was comparative the intensity assigned to metallic Sn on the surface of the droplet. However, after etching for 7min, only metallic Sn was observed at XPS sensitivity. The vacuum degree of 10^{-2}Pa strongly suggested formation of a relatively thick film of SnO_2 during the heat-treatment of the droplet. Therefore, it can conclude that the residual surface oxides of the tin droplet, which is a real shape of a sample to be etched in a new chamber, will be removed effectively. Moreover, the sputtering yield ratio of SnO_2/Sn/Fe is equal to 4.1/1.7/1 under the same conditions [18], [19]. It is expected that selective etching of surface tin oxides will proceed with negligible damage of surface of the iron rod that sustains the liquid bridge of tin.

Dissociation pressure of oxygen in the following equilibrium,

$$SnO_2 \text{ (solid)} = Sn \text{ (liquid)} + O_2 \qquad (3\text{-}1)$$

is the order of 10^{-30}Pa at a temperature level of the low Pr Marangoni experiments, 673K, [20]. The oxygen partial pressure (P_{O2}) of 10^{-30}Pa is an impossible level in a vacuum system with a present technology. Considering less heat loss from free surface of the melt by radiation, the vacuum condition has an advantage for carrying out the low Pr experiments, thus, we should investigate a prevention method of further oxidation not by equilibrium consideration but by kinetic aspects. Surface science of molten tin in vacuum conditions, combined with surface tension measurements, was studied by Auger electron spectroscopy (AES) [21]. As seen in Fig. 3-2, no contamination of molten tin surface by oxygen and no decrease in the measured surface tension values were found up to an oxygen exposure of 217 and 1.6×10^4 in Langmuir

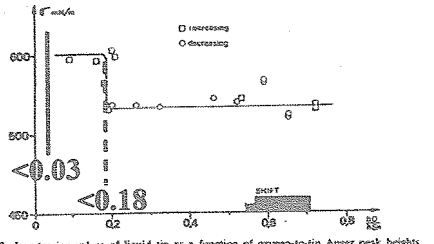

Fig. 2. Surface tension values of liquid tin as a function of oxygen-to-tin Auger peak heights. $T = 560 \pm 15$ K. (□) Data obtained by increasing oxygen exposure, (○) data obtained by etching an oxidized sample.

Data from R. Sangiorgi, et al., Surface Science, vol. 202 (1988) 509.

I_O/I_{sn}	O_2 exposure (L)	P_{O2}(Pa)
0.03	2.17×10^2	4×10^{-6}
0.18	1.60×10^4	5×10^{-2}

1L: exposure to gas corresponding to monolayer adsorption, ($1L=1.33\times10^{-4}$Pa×1sec).

In low Pr experiment,
Time for one experiment: about 2 h
(assumption: Sn → Sn oxides, Ea=20kcal/mol)

I_O/I_{Sn}	P_{O2} (Pa)	Possible exposure time at 560K	at 673K
0.03	**1×10^{-7}**	80 h	**3.9 h**
0.03	1×10^{-6}	8 h	0.4 h
0.18	1×10^{-6}	592 h	29 h

Specification of vacuum degree: $P_t=10^{-6}$Pa order

Fig. 3-2 Effects of oxygen exposure on oxidation of tin surface

unit, respectively, at around 560K (1L=1.33×10^{-4}Pa·s; corresponding to monolayer adsorption). The oxygen exposure of 217L corresponds to an exposure at P_{O2} of 1×10^{-7}Pa for 80h at 560K and at P_{O2} of 1×10^{-7}Pa for 3.9h at 673K by assuming that activation energy for the oxidation of molten tin reaction be 84kJ/mol. Since required time for one experiment in the low Pr study is about 2h, negligible alteration in surface tension will occur during a course of an experiment, leading to reliable and reproducible experimental data. It is concluded that prevention of further oxidation of molten tin will be possible in a vacuum chamber at a total pressure level of 10^{-6}Pa during one experiment.

3-2. Design and Specification of New Chamber

The new chamber mainly designed for obtaining required total pressure level of 10^{-6}Pa discussed in Section 3-1. The design was also included other required improvements extracted through experimental operation using the ex-chamber that was described in the previous issue [12]. These were molten tin supplying mechanism, temperature control mechanism of the liquid bridge, number and location of port for measurements, and panel material for lowering stray light from the chamber wall. The all improvements were carried out by minimum modification of the ex-chamber and equipment that has already installed.

Figure 3-3 shows the outline of structure and improvement points of the new chamber. The main features were as follows:

(1) The Ar^+ ion-etching gun, which was designed for surface cleaning and commercially available from VG Microtech, was newly installed at the parietal of the chamber. This etching gun aims the tin droplet on top of lower rod which can rotate in order to etch whole surface of tin.

(2) Performance of evacuation was attained to reduce the evacuation resistance by widening the piping diameter and the evacuating area by which the gate-valve was installed between the main chamber and the sub-chamber for melt supplying mechanism.

(3) The cooling mechanism for lower rod operated by He gas was newly installed in order to impose controlled temperature difference against the liquid bridge.

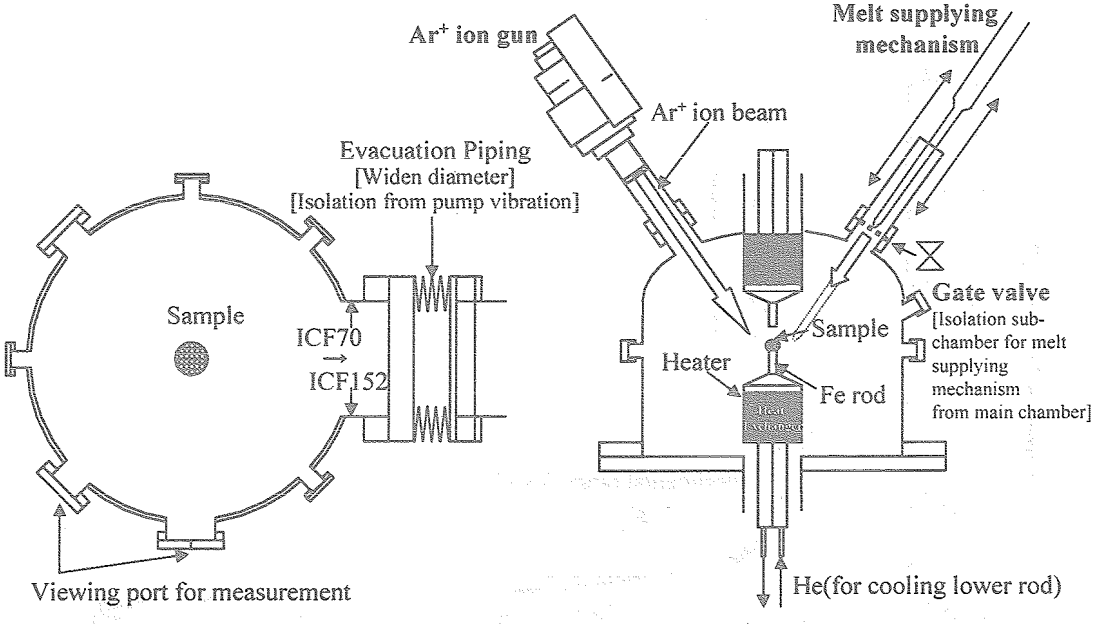

Fig. 3-3 Structure and main features of the new chamber

(4) Isotropic graphite pretreated with an acid was selected as the panel material for lowering stray light because of its low outgassing rate [22]. The panel had detachable mechanism from the chamber wall.

3-3. Performances of New Chamber

The measured performance of evacuation and Ar^+ ion etching are shown below. Figure 3-4 shows a performance of evacuation. The total pressure was reached level of 10^{-5}Pa, which is close to required level, for only 15min after evacuation started. Once the chamber degassed at around 570K (the chamber wall temperature was about 370K), the total pressure level of 10^{-6}Pa was obtained under same experimental conditions. Thus, the required vacuum degree was confirmed.

Fig ure 3-5 shows a change of O-atom ion concentration in the Ar^+ ion etching process of the droplet of solid tin. The total pressure was about 4×10^{-4}Pa during the etching and accelerating voltage of Ar^+ ion was 5kV. In order to etch all surface of the semi-spherical shape, the sample was manually rotated to $\pi/4$ radian after etching a given surface of the droplet for 3 to 5min, followed by the same etching processes (total etching time: 24 to 40 min). The concentration of O-atom, which is given as an ionic current, was measured by Quadruple Mass Spectrometer (QMS) that has been already installed in the experiment chamber. It was clearly shown that high sensitive monitoring of the etching process was possible with QMS.

Surface tension values before and after the etching of tin droplet was measured at 530K in order to estimate the effect of the etching on removal of residual surface oxides. Surface tensions were measured by the sessile drop method, and the measurements were carried out by collaboration with Prof. Mukai and Dr. Yuan of Kyushu Institute of Technology. The surface tension value was increased about 2% by the etching, strongly suggesting effectiveness of the etching for the surface cleaning. Figure 3-6 shows change in the surface tension values with time at 613K. However, the measured values were constant at around 504mN/m within an experimental error for the time of 55min. It was concluded that there was no appreciable surface oxidation of molten tin at a total pressure level of 10^{-6}Pa during one Marangoni experiment.

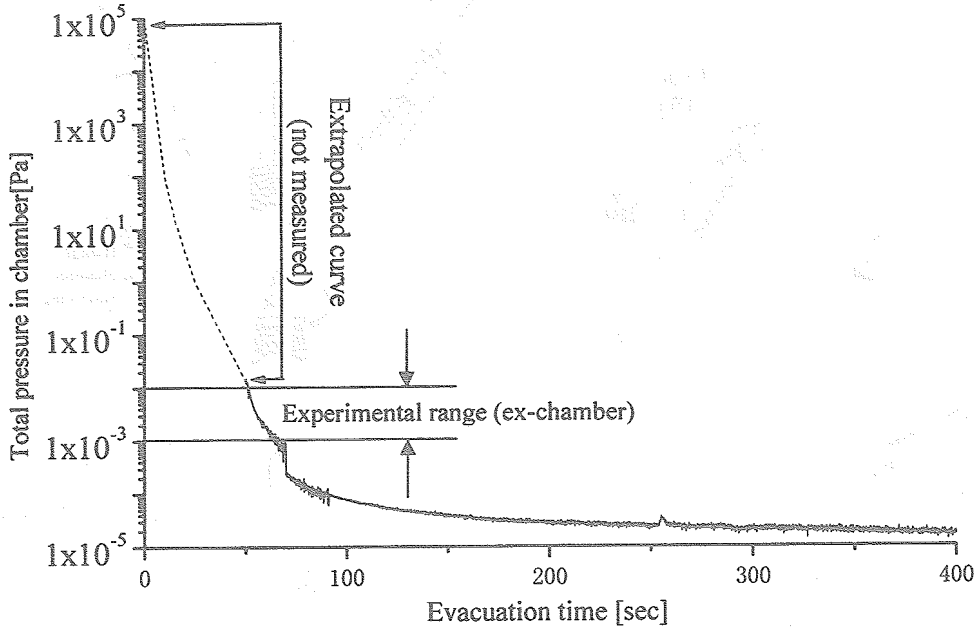

Fig. 3-4 Measured evacuation performance (before degassing)

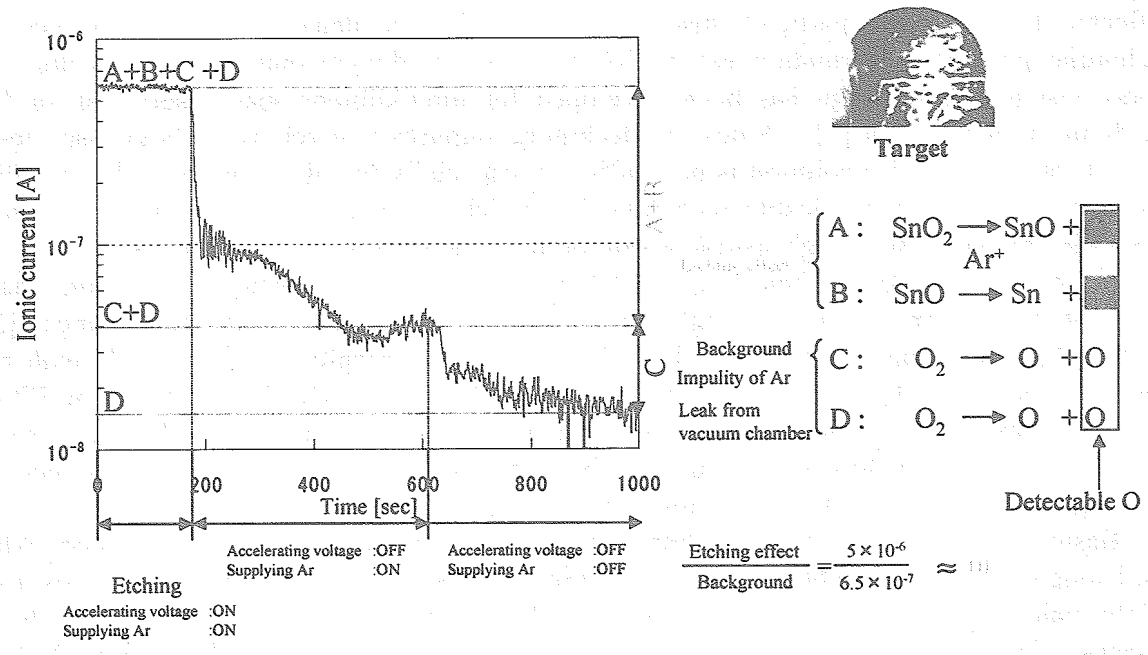

Fig. 3-5 Monitoring the Ar^+ ion etching process by QMS

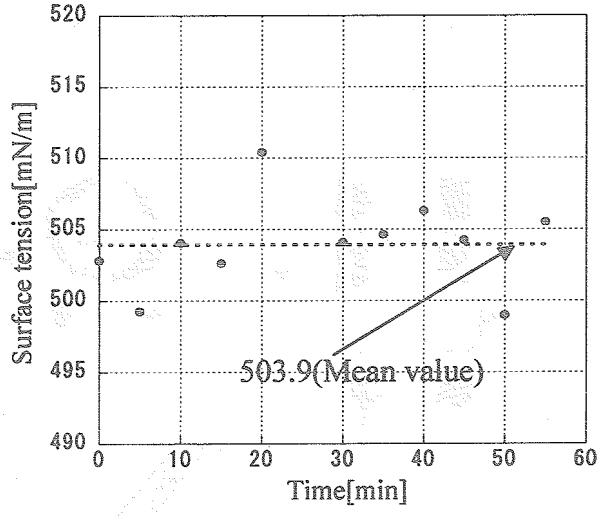

Fig. 3-6 Change in surface tension with time at 613K and 10^{-6}Pa (total pressure)

4. DEVELOPMENT OF MEASURING TECHNIQUE OF FLOW FIELD AND MANUFACTURING TECHNIQUE OF TRACER

4-1. General Aspects and Principles of Measuring Technique

Since the flow fields are not in accord with the temperature fields and the fluids are easily contaminated and/or oxidized by circumstances and probes, non-contact measurement of flow fields is very important for an experimental study of Marangoni flows. One of the available techniques is based on the principle by which the Doppler shift of an ultrasonic wave

reflected from moving particles suspended in the fluid is detected [23]. However, this technique provides information essentially about a one-dimensional velocity vector. An X-ray visualization system has been developed for three-dimensional observation of flow fields in molten silicon [2]. Since this technique requires that relatively large particles be suspended, the spatial resolution is not sufficient, especially for observation of the transition. To date, there is no applicable technique by which the flow fields are able to observe three-dimensionally with high spatial resolution for wide variety of liquid metals.

Novel visualization technique (3D-UV) of flow field measurements for liquid metals using ultrasonic transducer with high heat resistance is currently under development [24]. 3D-UV technique has potential for three-dimensional observation of flow fields with high spatial resolution. This section presents experimentally predicted performances of 3D-UV such as a resolution, a minimum size of a tracer, a signal processing method, and so on. 3D-UV requires development of unique balloon-like tracer. Design of the tracer and development of elemental technique for manufacturing the tracer is presented also.

Basic concept of 3D-UV is illustrated in Fig. 4-1. A number of the transducers, which are a single crystal of $LiNbO_3$ (LN), with Curie temperature of 1470K are attached over one of the pair at a certain distance from the interface between the rod and the liquid bridge because directivity of ultrasonic (US) beam makes wide. A principle of 3D-UV is as follows:

(A) The US beam transmitted from one transducer is reflected over a surface of a moving tracer suspended in the melt,

(B) Then, the echo beam can be received by the plural transducers simultaneously, leading to three-dimensional detection of a position of the tracer,

(C) Finally, the process (A) and (B) are repeated with a high frequency (a transmitting transducer is also scanned), resulting in visualization of a flow field of the melt.

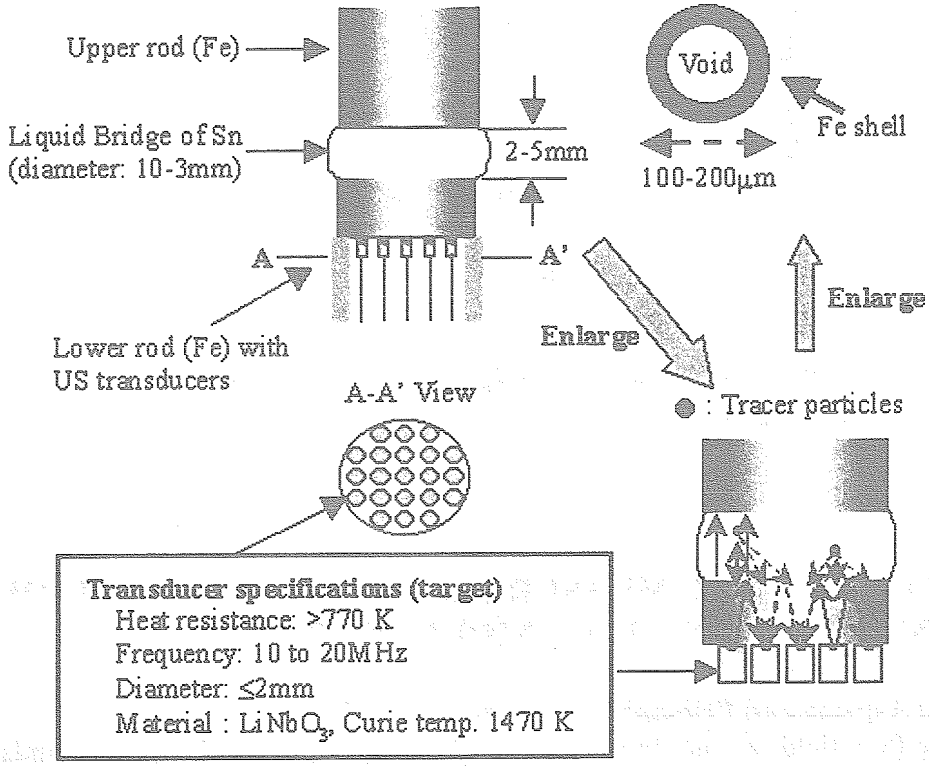

Fig. 4-1 Basic concept of novel three-dimensional ultrasonic visualization technique of flow field for liquid metals

4-2. Materials and Method

It is difficult to conduct an experiment for prediction of the performances in molten tin because the surface of the melt is easily oxidized in an atmospheric condition. Therefore, a model material for the rod and the fluid was used for the development of 3D-UV. Selection of the model material was based on its acoustic characteristics such as acoustic impedance (Z), transmittance (T), and reflectance (R). Definition of these values is as follows:

$$Z = \rho \cdot c \qquad (4\text{-}1),$$

$$T = \frac{4Z_1 Z_2}{(Z_1 + Z_2)^2} \qquad (4\text{-}2),$$

$$R = \sqrt{1 - T} \qquad (4\text{-}3),$$

where, ρ is a density and c is an acoustic velocity. Table 4-1 shows the materials used in this work. The conventional PZT transducer (lead zirconate titanate) was used only for a preliminary experiment.

Table 4-2 shows acoustic characteristics of the materials used in this work and the low Pr experiment for the Marangoni study. The values of T and R were calculated by the equations (4-2) and (4-3), respectively. Clearly, a glass plate and a hole are a good model for the fluid and the tracer, respectively, because of the same acoustic characteristics between them. This means high correlation can be expected between predicted performances from this work and true ones in the low Pr experiments. An experiment cell for this work was illustrated in Fig. 4-2. The hole was obtained by drilling the glass plate. Unfortunately, drilling a hole of 100μm was impossible, thus a hole of 300μm was a minimum tracer model. Depth of 12mm in the glass plate corresponds to depth of about 5mm in the liquid bridge of tin based on acoustic velocity ratio of both media. Glycerin paste was used as a couplant between the rod and the glass plate. An echo signal from the hole (*T*) was observed between an echo from the first interface (*S*) and an echo from the second one (*B*).

Table 4-1 Materials used in this work

Transducer (status)	Frequency (MHz)	Temp. (K)	Bonding method	Rod model	Fluid model
PZT (preliminary)	2	rt.	adhesion	acrylic resin	water
$LiNbO_3$ (target)	10-20	rt.	adhesion	Fe, Ti, steel	glass plate
$LiNbO_3$ (target)	10-20	773	soldering	Ti, steel	glass plate

Table 4-2 Acoustic characteristics of the materials used

	Low Pr experiment			This work		
	Material	Z (×10⁶) (kg/m²s)	T (%)	Material	Z (×10⁶) (kg/m²s)	T (%)
Fluid	Sn	17.6	-	Glass plate	15	-
Rod (1)	Fe	46.2	79.9	Fe, steel	46	74
Rod (2)				Ti	27.1	92
Tracer [1]	Fe-balloon	<0.4 [2]	R>95	Hole	4×10^{-4}	R~100

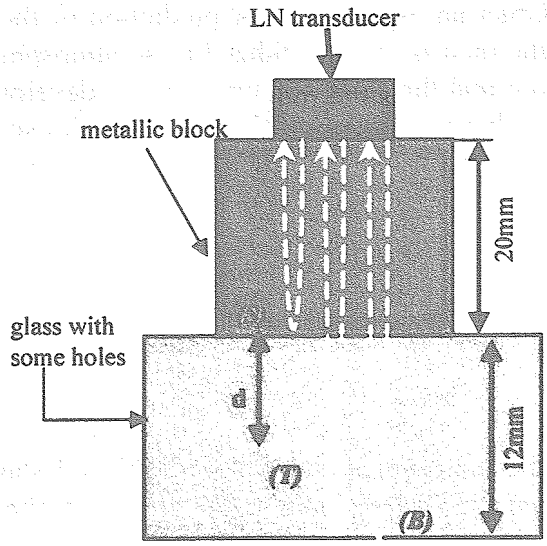

Fig. 4-2 Cell for model experiments using the glass plate with some holes (0.3-1.0mm in diameter, 2-10mm in depth)

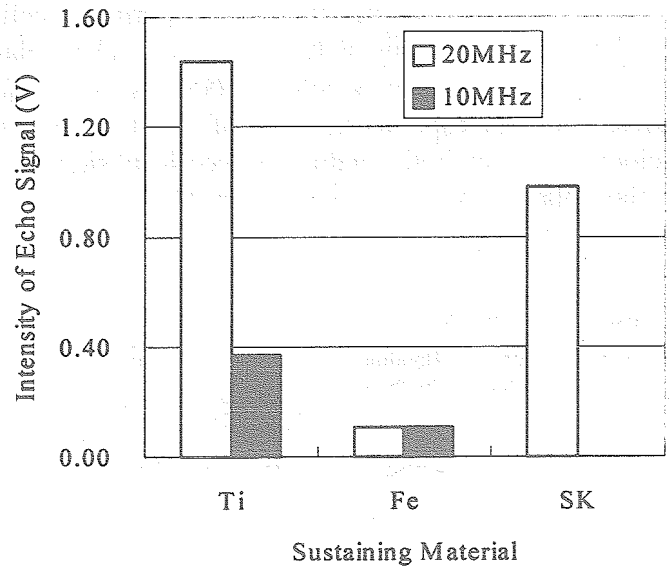

Fig. 4-3 Echo intensity changes with changing a rod material to sustain the liquid bridge of Sn

Intensity of the echo signal from *S* was measured with three materials for the rod. If the echo intensity from *S* is high, the US beam in the fluid will be intense, leading to a clear echo signal from *T*. In this experiment, the LN transducers attached by an epoxy resin were used for the room temperature measurements. The results are shown in Fig. 4-3, where SK is a sort of steel classified by Japanese Industrial Standard. The high intensity of the echo was obtained with Ti-rod and SK-rod, especially at frequency of 20MHz, whereas the intensity was drastically damped with Fe-rod. Microstructure of each rod materials was observed cross-sectionally by scanning electron microscope (SEM). As shown in Fig. 4-4, maximum crystallite size was about 50, 200, and 2μm for Ti, Fe, and SK steel, respectively. Since

wavelength of US is about 300μm in these metals, it is concluded that US beam was scattered in the large grain boundary of Fe, leading to extremely damping the intensity. The growth to large crystals of Fe in pure iron was unavoidable without additives such as P or B compounds. Therefore, Ti or SK was suitable as the rod material, of which a surface should be coated by Fe.

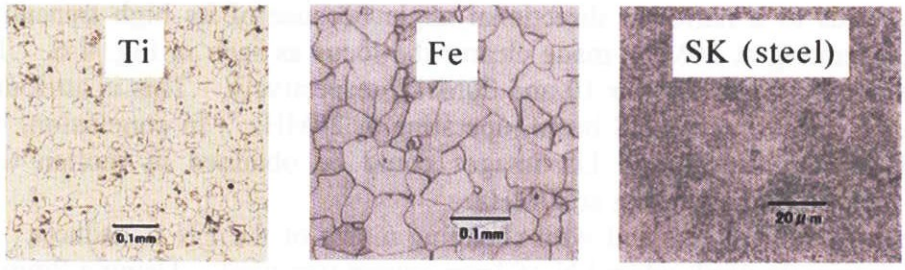

Fig. 4-4 Cross-sectional observation of the rod materials by scanning electron microscope. Maximum crystallite size is about 50, 200, and 2μm for Ti, Fe, and SK, respectively.

4-3. Prediction of Performances

If one moves the LN transducer over the glass plate horizontally, a distance between LN and one hole (*T*) changes, whereas distances between LN and *S*, and also LN and *B* are constant. Therefore, a locus like an arc will be observed only in the echo signal from *T* when US beam has a wide directional angle with sufficient strength. And such US beam can leads to high spatial resolution of the tracer position because an echo from the tracer can be received by a number of transducers.

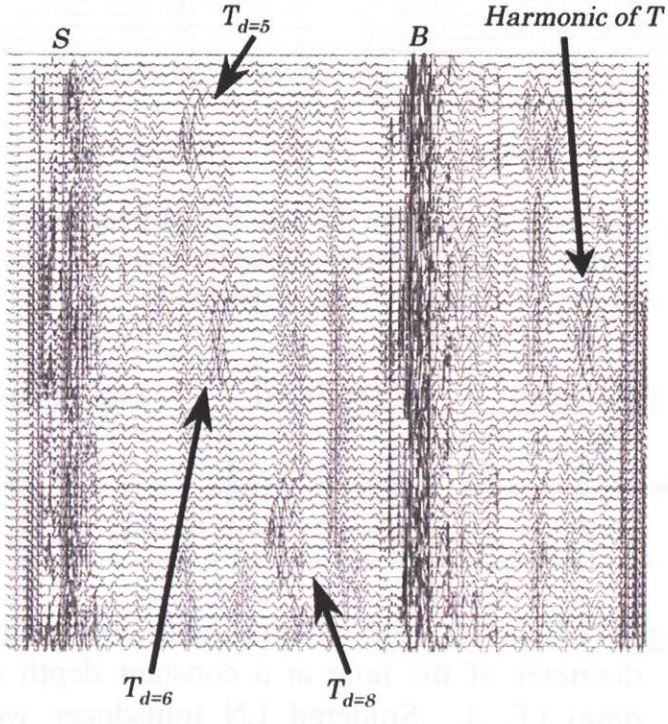

Fig. 4-5 Observation of echo signal locus at frequency of 10MHz

Three echo signal loci from three holes with the different depth ($T_{d=x}$) were successfully observed between the fixed echo at the receiving time of around 7μs (S) and same one at around 11μs (B) as shown in Fig. 4-5. The LN transducer attached over the rod by the epoxy resin was operated at frequency of 10MHz and was moved in a position every 1mm pitch in this experiment. The echo signal was recorded after 16 times integrating the received echo and calculating a difference between the echo and the background noise. In general, higher frequency leads to a narrower directional angle because of its high transmitting property. However, operating at 20MHz made clearer the locus as seen in Fig. 4-6. The directional angle was about 16 and 18° for 10 and 20MHz, respectively. This is attributable to higher S/N ratio, *i.e.* more intense US beam, operating at 20MHz. In conclusion, it was strongly suggested that high-resolution US images could be obtained in molten tin by aperture synthesis method [25] operating at 20MHz.

The echo intensity changed with changing a size of the LN transducer. The observed echo was extremely weak when LN of 1mm-square was used. Using a 2mm-square crystal is valid to obtain a wide directional angle and sufficient strength of US beam. Since a spatial resolution for an azimuthal position of the tracer (R_θ) depends on a number of transducers which can receive the echo, the present results can not predict the precise value of R_θ. Instead of the precise value, we can predict that the minimum value of R_θ is close to one half of the selected LN size, *i.e.* about 1mm, in case only one transducer can receive the echo. Actually, the results shown in Fig. 4-5 and 4-6 clearly suggest that multi-receiving-system can be designed, therefore, an actual value of R_θ will be a certain value between 1mm and the tracer size.

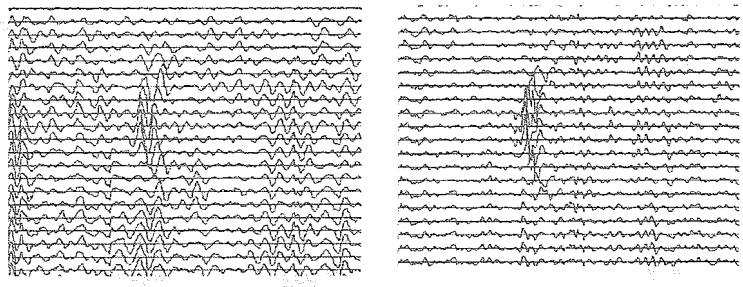

(A) 10MHz (B) 20MHz

Fig. 4-6 Echo locus from the hole $T_{d=5}$ at frequency of (A) 10MHz and (B) 20MHz. Directional angle is about 16 and 18° for 10 and 20MHz, respectively.

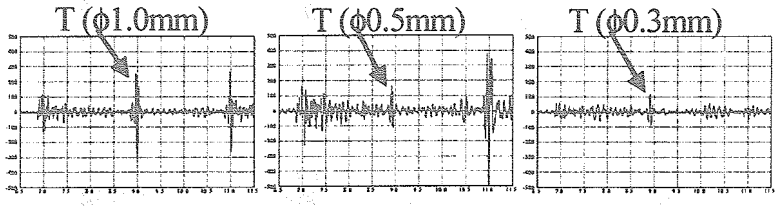

Fig. 4-7 Echo intensity changes with changing a diameter of the hole at a constant depth of 6mm ($T_{d=6}$). Soldered LN transducer was used for high temperature experiments.

Influence of a diameter of the hole on the intensity of the echo from T was examined. An example of the results using Ti-rod is shown in Fig. 4-7, where the diameter of the hole was expressed as "ϕ x mm." From this experiment, the soldered LN transducer was used for the high temperature experiments (773K). An aluminum alloy was used as solder. After soldering, the LN transducer was pre-treated at high temperature in an atmospheric condition for about two weeks. The echo signal was recorded after 16 times integrating the received echo and calculating a difference between the echo and the background noise. The echo intensity decreased with decreasing the diameter of the hole, and the same tendency in the intensity was observed using another rod. From these results, we can predict intensity of the echo from the hole of 0.1mm in diameter, which was not able to drill, as described below.

All experimental values of the echo intensity using various rod materials and the holes (0.3, 0.5, and 1.0mm in diameter) were plotted against the hole diameter as shown in Fig. 4-8, where the echo intensity was expressed as a relative intensity to the intensity recorded using the hole of 0.5mm. The solid line shows that linear correlation between the relative intensity and the hole diameter can observe at the constant depth of 6mm. By the solid line, the relative intensity of the echo from the hole of 0.1 and 0.2mm can be predicted as seen in Fig. 4-8.

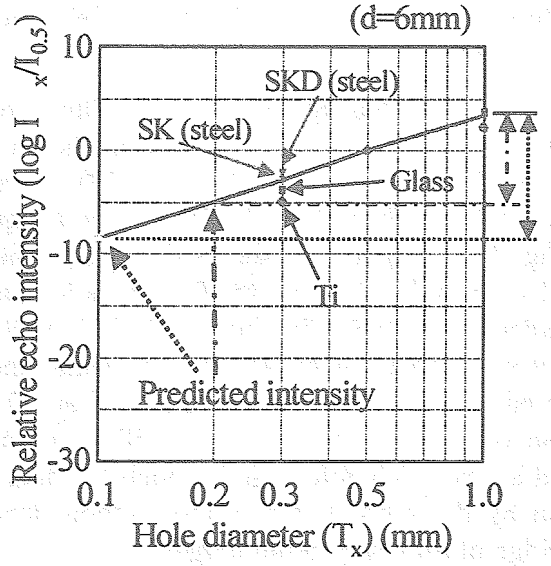

Fig. 4-8 Relationship between the relative echo intensity and the hole diameter at the depth of 6mm

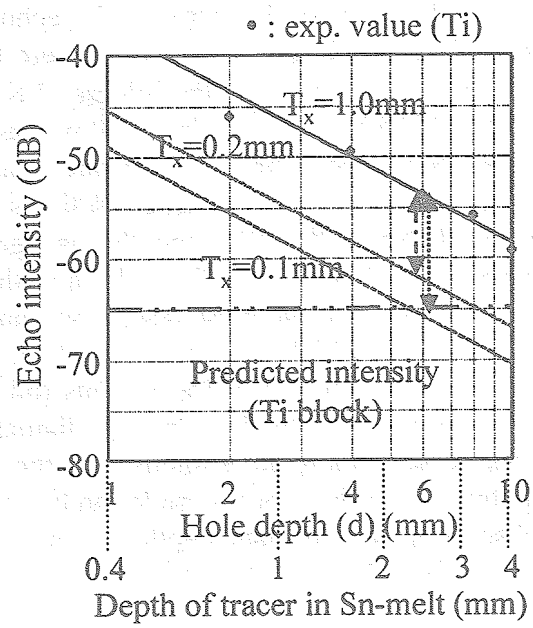

Fig. 4-9 Prediction of echo intensity from a hole with a diameter of 0.1 and 0.2mm at any depth

The echo intensity, which was recorded from the hole of 1.0mm in diameter at 2-10mm in depth with Ti-rod, was damped with the depth of the hole as shown in Fig. 4-9. The echo intensity from the hole of 2mm depth was too strong to amplify the signal linearly, resulting in saturation in the output intensity. Therefore, all data can be adequately approximated by the solid line as shown in Fig. 4-9. Figure 4-8 shows that the predicted difference between the echo intensity from the 1.0mm hole and from the 0.2mm hole is about –9dB at the depth of 6mm. Also, we can predict the intensity for the 0.1mm hole will decrease about –12dB. The dashed lines in Fig. 4-9 were obtained by shifting the solid line by –9dB and –12dB, respectively, leading to the predicted echo intensity from the 0.2 and 0.1mm hole at any depth. The lower limit of detection of a signal was about –65dB experimentally by the present processing method described above. Therefore, it is concluded that the minimum diameter of the tracer is 0.2mm even by the present processing method, leading to the flow fields visualization of the liquid bridge of Sn with 3.5mm height.

Trial productions of multi-transducer-system were carried out by the method illustrated in Fig. 4-10, in which four LN transducers were integrated ("quadri-LN-system," hereafter). Large crystal (5mm square) was soldered over the metallic block surface, subsequently cut into 2mm-square one. Using a large crystal resulted in precise soldering of LN; thus the echo signal from S of the glass plate was more intense (about 6dB) by using the quadri-LN-system than the single-LN-system as seen in Fig. 4-11. However, the echo intensity decreased about 2dB in molten tin at 723K than the same one observed with the glass plate. Therefore, it is concluded that the echo intensity in molten tin will be improved about 4dB (+6-2) than the intensity shown in Fig. 4-9 by using the quadri-LN-system. This means the tracer of 0.15mm in diameter will be able to detect at 4mm in depth of the liquid bridge of Sn, leading to satisfactory experimental conditions for the flow visualization in which the aspect ratio (As) will be a range of 2.3 (a=1.5mm) to 0.8 (a=5mm).

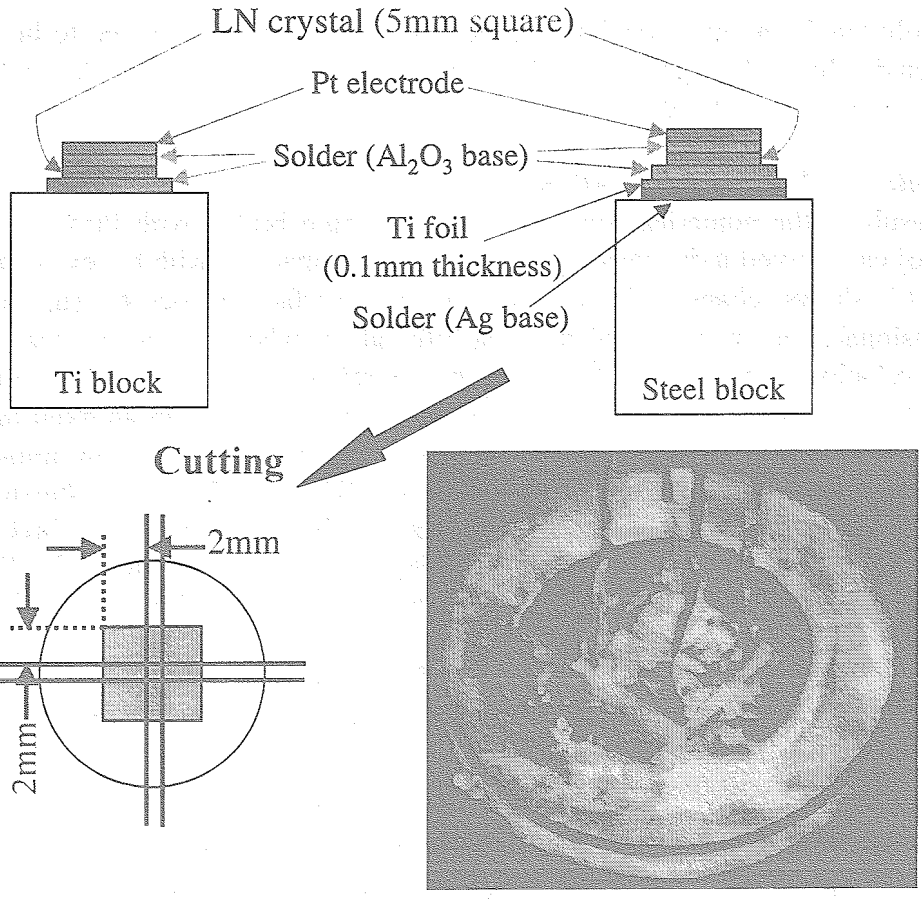

Fig. 4-10 Preparation method of multi-transducer-system

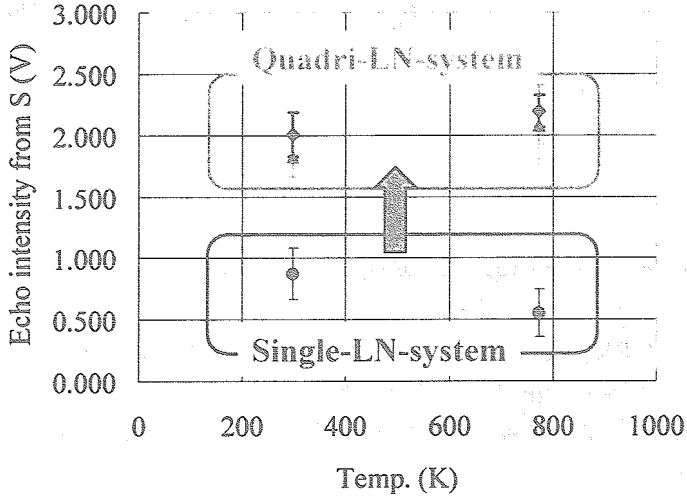

Fig. 4-11 Improvement of echo intensity
by using "quadri-LN-system"

Since a positive region of US waveform will digitize for the signal processing, an axial position of the tracer will have a maximum error of one half of wavelength of US in the melt. The wavelength of US operating at frequency of 20MHz is about 120μm in molten tin, thus a

spatial resolution for an axial position of the tracer (R_z) can be predicted to be about 60μm. The predicted value of R_z is reasonable because 60μm is smaller than the detectable minimum size of the tracer (200-100μm).

4-4. Detection of the First Bifurcation

The result of the numerical simulation of the liquid bridge with Pr=0.01, Ma=50, and As=1.0 [26] can convert a *dimensional-plot* for easy comparison with the experimental results. Figure 4-12 shows changes in the *dimensional* surface velocities (u_z and u_θ) with non-dimensional time (τ) at around the first bifurcation, where u_z and u_θ mean an axial and azimuthal velocity, respectively. Since a sampling rate of 3D-UV is designed in the order of 10μs, an axial and azimuthal velocity resolution would be less than an axial and azimuthal position resolution (R_z and R_θ) predicted above, respectively. The flow transitions at the first bifurcation can detect with high precision by the 3D-UV technique as shown in Fig. 4-12. Therefore, it is concluded that the 3D-UV technique has advantages for three-dimensional observation of flow fields of the liquid bridge than the conventional ones [2], [23], especially for studying the transition phenomena of Marangoni convection, and that 3D-UV should be developed further.

The present studies were conducted for the ground-based experiments. For a space experiment, further miniaturization of the transmitting and receiving unit of US and measuring instrument should be developed.

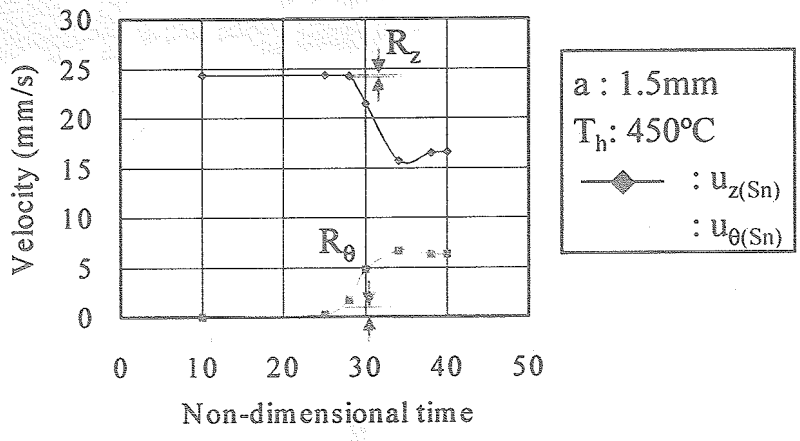

Fig. 4-12 Changes in *dimensional* velocities with non-dimensional time
ΔT=6.8K, T_h=723K, $(T_h+T_c)/2$=719.6K, a=1.5×10^{-3}m,
α=2.17×10^{-5}m^2/s (at 719.6K),
u=U α/a (u: *dimensional* surface velocity, U: non-dimensional surface velocity)

4-5. Development of Tracer

For obtaining high signal to noise ratio, a tracer for 3D-UV needs to have high reflectance of US beam. Since the target value of the reflectance is up to 95%, as seen in Table 4-2, acoustic impedance of a tracer should be less than 0.4×10^6 kg/m^2/s by the equations (4-2) and (4-3). Considering the equation (4-1), this impedance value is only attainable to make a tracer balloon-like structure because acoustic velocity is about 2,570m/s in molten tin and bubbles are not able to suspend in the melt under normal gravity. Now, we propose a very unique feature of the balloon tracer that can be actually manufactured.

The balloon tracer should have following characteristics: high thermal stability, high wettability and low reactivity against molten tin, and high sphericity in a shape. The high wettability and low reactivity requires an iron shell on which the tracer contacts with the melt. However, welding a thin plate of iron is not feasible for manufacturing the balloon, of which the target diameter is 0.15mm as discussed in Section 4-3, because a special tool for handling and processing a thin plate should be developed for manufacturing the small balloon. It is most feasible way for manufacturing the tracer that surface of an available porous or balloon-like raw material is modified by an iron layer. Such raw materials are listed and compared qualitatively in Table 4-3. Selection of Shirasu-balloon (SB), which is an expanded volcanic particle, as the raw material is reasonable because SB shows high thermal stability and is available with near target diameter [27].

Table 4-3 Qualitative evaluation of balloons and porous materials

	Sphericity	Available size (μm)	Capability to maintain its void in melt	Heat resistance at 773K	Total evaluation
porous SiO_2	○	1~150, ○	×	○	×
porous glass	○	100~500, ×	?	△	×
Shirasu-balloon	△	10~1000, ○	○	○	○
pearlite	×	>150, ×	×	○	×
glass balloon	○	10~100, ○	○	△	△
Al_2O_3 bubble	×	?	?	○	×
TiO_2 balloon	○	30~50, ×	?	○	×

Shirasu: glassy volcanic fragment distributed in southern Kyushu, also named Hakudo.

Since density of the tracer has to be close to that of molten tin (about 6.9×10^3 kg/m^3 at 673K) for a ground-based experiment, thickness of an iron layer should be 30-40μm. In general, thickness of a film that can be grown by sputtering is only few microns. Therefore, surface modification of SB should carried out by plating of Fe. Since SB shows excellent electric insulation and electroless plating of Fe is impossible, the plating should be conducted as following processes:

1st: Electroless plating of Ni (Ni/SB)

$$Ni^{2+} + H_2PO_2^- + 3OH^- \rightarrow Ni + HPO_3^{2-} + 2H_2O \quad (4\text{-}4)$$

2nd: Electrolysis plating of Fe (Fe·Ni/SB)

$$Fe^{2+} + 2e^- \rightarrow Fe \quad (4\text{-}5)$$

By simple calculation, overall features of the tracer (about 150μm in diameter) will be as follows: diameter of SB is 90-100μm and thickness of plating layers of Ni and Fe are 10-15μm and 10-20μm, respectively.

Elemental techniques that should be developed are a method to improve sphericity of SB and plating conditions to obtain flat surface of Ni and Fe. In 1999, we have mainly studied development of the plating techniques. Since using a small particle of SB (*i.e.* 90-100μm) makes it difficult to handle the particles for the plating and to analyze a plating layer, 1000μm-class SB, which is produced as an expanded perlite by Fuyolite Co. Ltd. and named

"Fuyolite #1", was used for the development. Sphericity of Fuyolite #1 was not good; thus flatness of the plating layer has been often affected by shape of Fuyolite #1 itself. However, cross-sectional observations by optical microscope (OM) and scanning electron microscope (SEM) have enabled us to resolve whether the flatness has been affected by the shape of Fuyolite #1 itself or not. Sphericity of 100μm-class SB have improved to some extent by preliminary experiments, however, details of the results will be published in the next issue.

The trial experiment was conducted for electroless plating of Ni over the 1000μm-class SB as shown in Fig. 4-13 ("Ni/SB #1," hereafter). In this experiment, a plating solution ($NiSO_4$ aqueous solution) and a reducing agent for Ni^{2+} (NaH_2PO_2) were simultaneously added dropwise to SB dispersed mechanically in water, in which molar ratio of $H_2PO_2^-/Ni^{2+}$ was kept constant at three. The equation (4-4) is an equimolar reaction, hence, the degree of excess of $H_2PO_2^-$ in a reaction vessel will become larger in the course of the plating, resulting in accumulation of unreacted $H_2PO_2^-$ in the plating layer by physical adsorption. SEM images clearly showed that columnar crystal growth took place whole period of the reaction. Elemental analyses of the plating layer by Auger electron spectroscopy (AES) revealed that nickel oxide(s) of 5nm in thickness existed on the surface and high concentration of Na in the bulk.

Electrolysis plating of Fe was carried out over Ni/SB #1 sample by using $FeSO_4$, H_2SO_4, and H_3BO_3 electrolyte and a basket-type galvanic cell (Fig. 4-15). However, no plating took place over Ni surface of the sample.

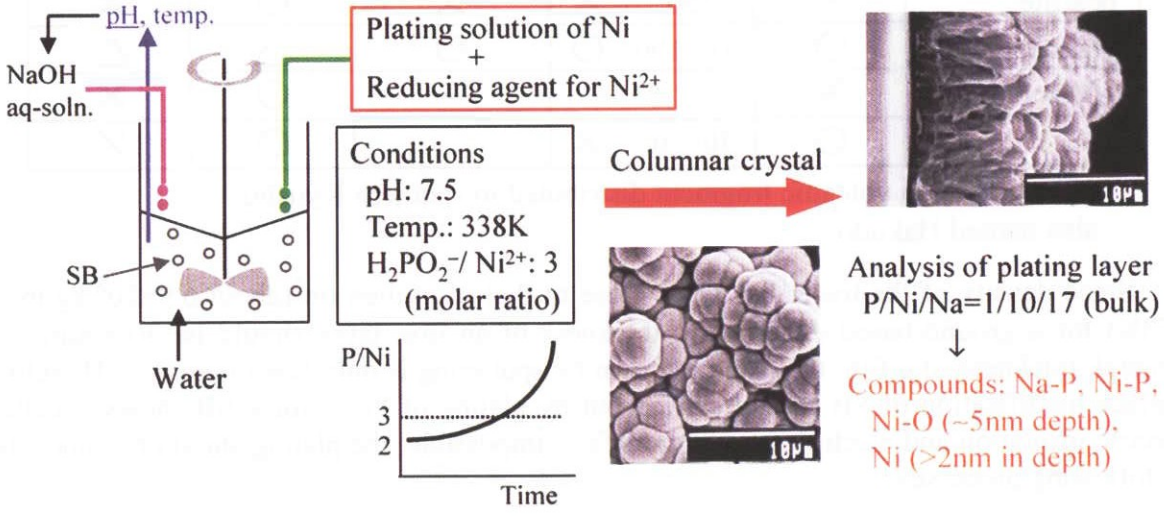

Fig. 4-13 Trial experiment of electroless plating of Ni over 1000μm-class SB
Plating solution and reducing agent were simultaneously added.

It is well known that columnar crystal growth often take place under high concentration of $H_2PO_2^-$ and passivity of Ni-oxide film increase with content of $H_2PO_2^-$. Therefore, the feeding method of the plating and reducing agent of Ni^{2+} should be improved for lowering the concentration of $H_2PO_2^-$. However, secondary surface oxidation is unavoidable for Ni/SB because nickel is a base metal and Ni/SB has to handle for the next process, the plating of Fe. And high conductivity is required for electrolysis plating; thus, corrosive property should be increased by addition of hydrochloric acid (HCl) to the electrolyte of Fe plating.

Figure 4-14 shows the improved method for the plating of Ni. The 1000μm-class SB was dispersed in $NiSO_4$ aqueous solution (0.095mol/l) and only the reducing agent (NaH_2PO_2) were added dropwise to the reaction vessel at a constant pH of 6 ("Ni/SB #2,"

hereafter). The overall molar ratio of $H_2PO_2^-/Ni^{2+}$ was also three, however, it was easily inferred from the dropping method that the real ratio in the vessel approached zero in the initial period of the plating. SEM images clearly showed that layer by layer growth of Ni crystal proceeded almost whole period of the reaction and thickness of the plating layer was about 10-20μm. The columnar crystal was observed only on the surface of Ni/SB #2. This was attributable to high concentration of $H_2PO_2^-$ in the final period of the plating; thus, no columnar growth will be able to attain by further improvement of the feeding conditions, leading to flat surface of Ni/SB. AES analyses of the plating layer revealed that thickness of Ni-oxide(s) film decreased to 1.6nm and metallic Ni also existed on the surface.

The improved method for the plating of Fe is shown in Fig. 4-15. For increasing corrosive property, a mixed electrolyte of $FeSO_4$ and $FeCl_2$ (9/1 in molar ratio) was used in mixed acidic medium of HCl and H_3BO_3 (pH<2.0). Moreover, a number of the brass balls (2mm in diameter) were added to the basket-type galvanic cell, in which the ratio of the balls to the particles of Ni/SB #2 was about 5/1, for improvement of contact efficiency of Ni/SB #2 with the electrode. As a result, the electrolysis plating of Fe successfully proceeded over Ni surface in the cell rotating at 10rpm for 20-30min ("Fe·Ni/SB #1," hereafter). SEM images clearly showed that flat surface of Fe was obtained over Ni/SB #2 particle with the flat surface of Ni, whereas hill-like growth took place on the surface columnar crystal of Ni/SB #2. A particle having some pores on the surface was also seen. AES analyses of the plating layer revealed that thickness of surface oxide, which existed as FeO, was about 0.2μm and metallic iron shell was obtained with high purity (>99%) and 10-20μm in thickness in the bulk as seen in Figs. 4-15 and 4-16. Although there was inter-particle ununiformity of thickness and surface morphology of Fe plating layer, the ununiformity will be improved by improvement of the feeding conditions for the electroless plating and by further development of the electrolysis conditions in which rate of electrolysis can control.

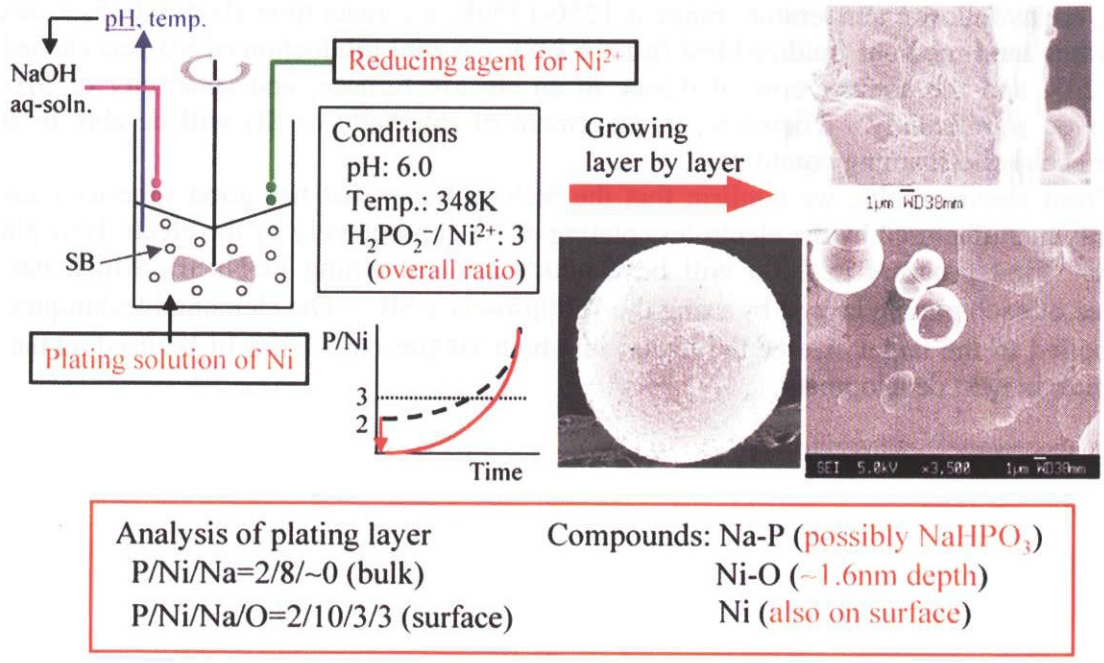

Fig. 4-14 Improved method for electroless plating of Ni
Only reducing agent was added.

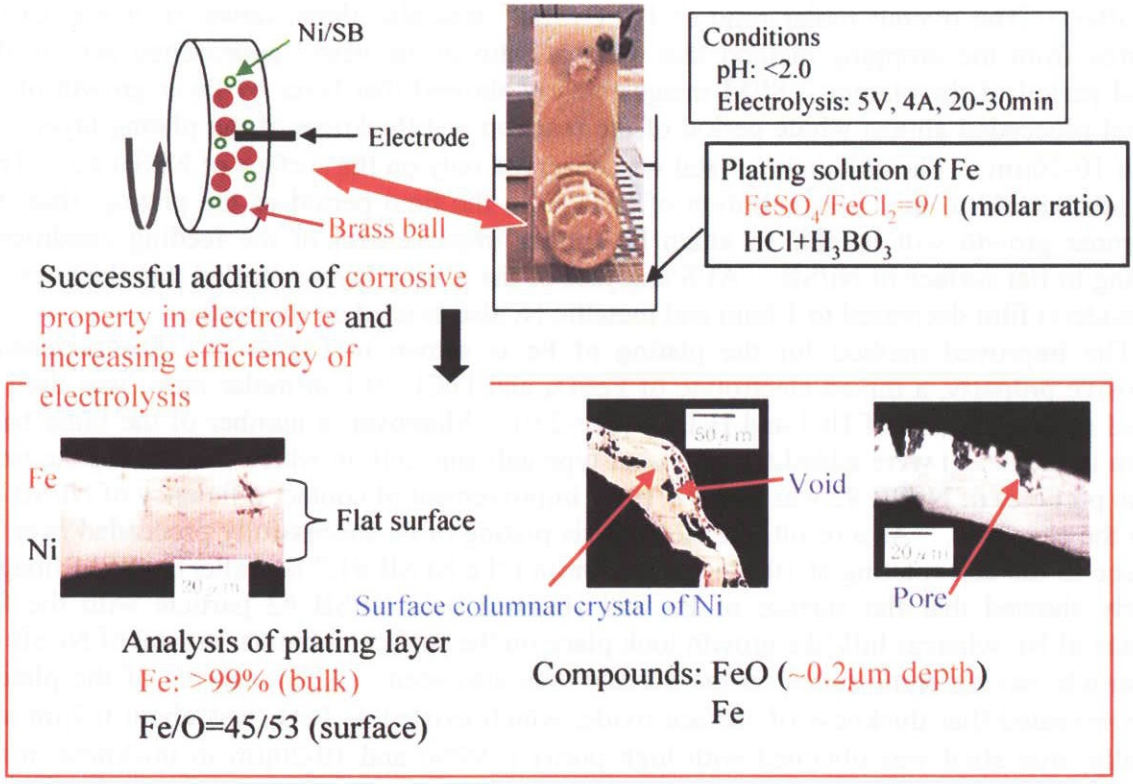

Fig. 4-15 Apparatus, conditions, and results of eletrolysis plating of Fe over Ni/SB

The conventional foaming conditions for manufacturing SB, of which sphericity is not good, are as follows: temperature range is 1250-1350K, a contact time about 0.025sec, and an apparatus sand-medium fluidized bed furnace [28]. A trial production of SB was carried out at 1520K and the contact time of 0.3sec in an electric furnace, and sphericity of SB was improved significantly. Therefore, improvement of sphericity of SB will be able to attain under such mild foaming conditions.

From above results, we confirm that the balloon tracer that has good sphericity can be actually manufactured by the electroless plating of Ni, subsequently by the electrolysis plating of Fe. First progress in 2000 will be conducted for obtaining Fe·Ni/SB, which has flat surface of each plating layers, by using the 1000μm-class SB. The elemental techniques will be applied to the target size of the tracer, in which 100μm-class SB will be used as the raw material, in next development.

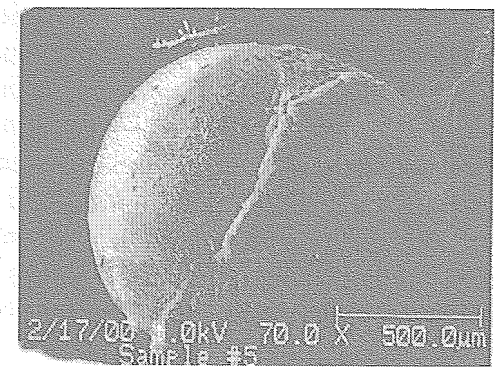

(a) SEM image of Fe•Ni/SB #1

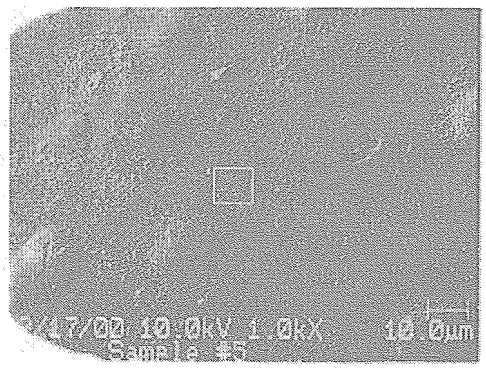

(b) Sputtering position for AES analysis

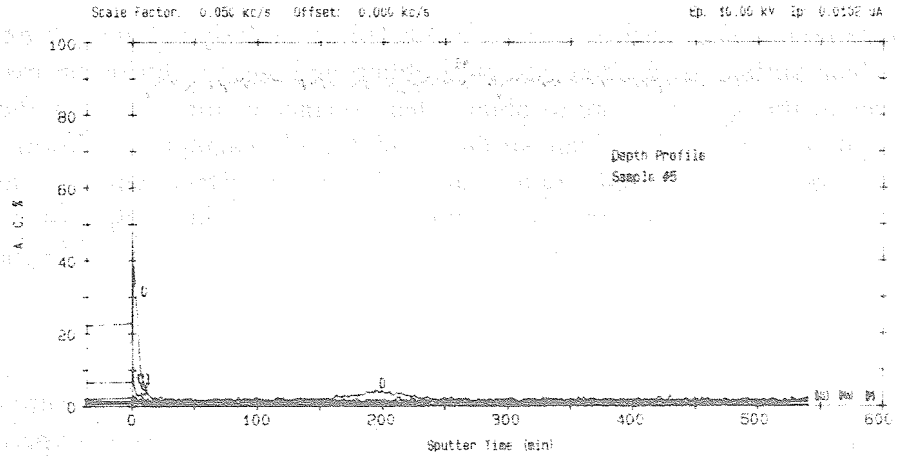

(c) Depth profile of elements in the plating layer of Fe

Fig. 4-16 AES analysis of Fe•Ni/SB #1 sample

5. CONCLUSIONS

The following conclusions were obtained from the present experimental studies.

(1) Measurement technique of surface temperature was developed. Theoretical radiation energy was calculated at a constant emissivity for reinvestigation of radiation thermometer. PbS photo detector can detect proper wavelength range (2.0~2.8μm) with high radiation energy, combined with use of CaF_2 optical pass filter, for the low Pr experiment. Moreover, the PbS photo detector has sensitivity approximately ten times higher than that of the HgCdTe which was the selected detector for previous measuring system. It was concluded that PbS photo detector (IMPAC Electronic GmbH, IP10/MB5) was optimum measuring instrument and surface temperature data with fine signal to noise ratio was expected by this system. The selected radiation thermometer had temperature resolution that was smaller than amplitude of temperature fluctuation at oscillatory thermocapillary flow by applying Japan Industrial Standard for radiation thermometer.

(2) The new measuring technique made it possible to observe surface temperature fluctuations of molten tin successfully near the second bifurcation point by using the ex-chamber in which CaF_2 optical pass filter has not been installed. The time series of surface temperature measured by the radiation thermometer indicated existence of standing

wave with very small amplitude but with distinguishable one. Amplitude of the fluctuation was larger than temperature resolution of the thermometer. The periodic fluctuation continued approximately 100sec, then damped gradually, suggesting that reduction of temperature coefficient of surface tension be caused by oxidation of fluid surface. Numerical simulation under conditions just same as the experiment showed that the calculated temperature difference (7.1K) at onset point was in good agreement with the experimental result (7.6K), while the calculated frequency (2.6Hz) was estimated 15 times larger than the experiment (0.17Hz). More precise results of temperature fluctuation with multi-point temperature measurements will be obtained by the promising technique of surface temperature measurement in conjunction with using a new experimental chamber where clean surface of molten tin is obtained and sustained during an experiment. Surface tensions of molten tin in the new chamber were studied by *in site* measurements. Research procedure, an experimental setup, and a method were presented.

(3) Considerations concerning surface science of tin led us to design of unique experiment apparatus where clean surface of molten tin could obtain and sustain during an experiment. The unique features of the apparatus are to obtain clean surface of molten tin by the Ar^+ ion etching method and to sustain the clean surface under high vacuum condition (10^{-6}Pa). Effectiveness of the apparatus for obtaining and sustaining clean surface was confirmed by *in situ* surface tension measurements and real images of the liquid bridge of tin. The multi-windows of the chamber were able to measure surface temperature fluctuations at different points of the liquid bridge simultaneously, leading to observing oscillation behavior by Marangoni flow.

(4) Performances of novel visualization technique (3D-UV) of flow field measurements for liquid metals using ultrasonic transducer with high heat resistance were experimentally predicted. The experiments were conducted with model materials based on the acoustic characteristics. The predicted performances were as follows: the spatial resolution for an axial position of a tracer was about 60μm, the minimum spatial resolution for an azimuthal position of a tracer 1000μm, the detectable minimum diameter of the tracer in molten tin 150μm, and aperture synthesis method feasible. 3D-UV can visualize flow field of the liquid bridge in which the aspect ratio is a range of 2.3 (a=1.5mm) to 0.8 (a=5mm). From comparative study with the numerical result by Prof. Imaishi et al., it was concluded that the flow transitions at the first bifurcation could detect with high precision by the 3D-UV technique.

(5) The visualization technique required development of unique balloon-like tracer. Shirasu-balloon, which is an expanded volcanic particle, is used as the raw material for the tracer and coated with iron shell. Elemental techniques that should be developed were a method to improve sphericity of Shirasu-balloon and plating conditions to obtain flat surface of Ni and Fe, and these were experimentally developed. It was confirmed that the tracer that has good sphericity could be actually manufactured by electroless plating of Ni over Shirasu-balloon surface, subsequently by electrolysis plating of Fe. Overall features of the tracer (about 150μm in diameter) will be as follows: diameter of Shirasu-balloon is 90-100μm and thickness of plating layers of Ni and Fe are 10-15μm and 10-20μm, respectively.

ACKNOWLEDGMENT

The authors would like to thank Dr. Sakuma (National Research Laboratory of Metrology) for his valuable advice for correction of radiation thermometer, as well as Mr. Yamamoto (NASDA) for his cooperation in measuring resolution of the thermometer. The authors are very grateful to Prof. Imaishi and Dr. Yasuhiro (Kyushu University) for understanding purpose of which that numerical simulations of low Pr fluid be conducted by us and modifying their program for enabling us to deal with dimensional values as input and output data by Dr. Yasuhiro. We are also grateful to Dr. Imai (Ishikawajima-Harima Heavy Industries Co., Ltd.) for his preliminary studies at NASDA.

REFERENCES

[1] Nakamura, S., Hibiya, T., Kakimoto, K., Imaishi, N., Nishizawa, S., Hirata, A., Mukai, K., Yoda, S., and Morita, T.: Journal of Crystal Growth, Vol. 186 (1998) pp. 85.

[2] Hibiya, T., Nakamura, S., Imaishi, N., Mukai, K., Onuma, K., Dold, P., Cröll, A., Benz, K-W., and Yoda, S.: "Marangoni Flow of Si Melt: Microgravity Experiments and Perspective," Proceedings of the Joint 1st Pan-Pacific Basin Workshop and 4th Japan-China Workshop on Microgravity Sciences, 8-11 July (1998) Tokyo.

[3] Han, J., Sun, Z., Dai, L., Xie, J., and Hu, W.: "Experiment on the Thermocapillary Convection of a Mercury Liquid Bridge in a Floating Half Zone," Journal of Crystal Growth, Vol. 169 (1996) pp. 129-135.

[4] Mukai, K., Yuan, Z., Nogi, K., and Hibiya, T.: "Effect of the Oxygen Partial Pressure on the Surface Tension of Molten Silicon and Its Temperature Coefficient," ISIJ International, Vol. 40 (2000) Supplement, pp. S148-S152.

[5] Cheng, M. and Kou, S.: "Thermocapillary Convection in a Low-Pr Material under Simulated Reduced Gravity," Proceedings of 4th Microgravity Fluid Physics & Transport Phenomena Conference (1998).

[6] Imaishi, N., Yasuhiro, S., Sato, T., and Yoda, S.: "Three Dimensional Numerical Simulation of Oscillatory Marangoni Flow in Half-Zone of Low Pr Fluids," Proceedings of 44th SPIE Annual Meeting and Exhibition, Materials Research in Low Gravity II, Vol. 3792 (1999) pp. 344-352, Denver.

[7] Kuhlmann, H.: "Hydrodynamic Instabilities in Thermocapillary Flows," Microgravity Science Technology VII/2 (1994) pp. 75-82.

[8] Chen, G., Lizee, A., and Roux, B.: "Bifurcation Analysis of the Thermocapillary Convection in Cylindrical Liquid Bridges," Journal of Crystal Growth, Vol. 180 (1997) pp. 638-47.

[9] Rupp, R., Müller, G., and Neumann, G.: "Three-Dimensional Time Dependent Modeling of the Marangoni Convection in Zone Melting Configuration for GaAs," Journal of Crystal Growth, Vol. 97 (1989) pp. 34-41.

[10] Levenstam, M. and Amberg, G.: "Hydrodynamic Instabilities of Thermocapillary Flow in a Half Zone," Journal of Fluid Mechanics, Vol. 297, pp. 357-372.

[11] Leypoldt, J., Kuhlmann, H., and Rath, H.: "Three-Dimensional Numerical Simulation of Thermocapillary Flows in Cylindrical Liquid Bridges," Journal of Fluid Mechanics, submitting.

[12] Imai, R., Takagi, K., Ohtaka. M., Ohtsubo, F., Natsui, H., and Yoda, S.: "Experimental Study of Thermocapillary Flow in the Half-Zone Liquid Bridge of Low Prandtl Number Fluid" (NASDA-TMR-990007E), National Space Development Agency of Japan (1999) pp. 71-113.

[13] The Japan Society of Mechanical Engineers: "New Measurement Method for Thermal-hydraulics," Yokendo (1998) pp.12-13.
[14] The Japan Society of Mechanical Engineers Data Book: "Heat Transfer 4th Edition," Maruzen (1986) p.296.
[15] Tao, Y. and Kou, S.: "Thermocapillary Convection in a Low-Pr Material under Simulated Reduced Gravity Conditions," Proceedings of 2nd Microgravity Fluid Physics & Transport Phenomena Conference (1996)
[16] Imaishi, N. and Yasuhiro: Private Communications (1999).
[17] Mukai, K. and Yuan, Z.: "Effects of Boron and Carbon on the Surface Tension of Molten Silicon under Precisely Controlled Oxygen Partial Pressure," Materials Transactions, JIM, Vol. 41 (2000) pp. 331-337.
[18] Almen, O. and Bruce, G.: Nuclear Instrumentation Methods II (1961) pp.257-279.
[19] Kelly, R. and Lam, N.Q.,: Redat. Eff., Vol.19 (1973) pp. 39.
[20] Passerone, A., Ricci, E., and Sangiorgi, R.: "Influence of Oxygen Contamination on the Surface Tension of Liquid Tin," Journal of Materials Science, Vol. 25 (1990) pp. 4266-4272.
[21] Sangiorgi, R., Senillou, C., and Joud, J.C.: "Surface Tension of Liquid Tin-Oxygen Alloys and Relationship with Surface Composition by Auger Electron Spectroscopy," Surface Science, Vol. 202 (1988) pp. 509-520.
[22] Okada, M., Fukuda, S., and Yamashina, T.: "Development of Complex Apparatus for Measurement of Outgassing Rate from Carbon Materials (in Japanese)," TANSO, Vol. 97 (1992) pp. 176-183.
[23] Takeda, Y.: "Measurement of Velocity Profile of Mercury Flow by Ultrasound Doppler Shift Method," Nuclear Technology, Vol. 79 (1987) pp. 120-124.
[24] Takagi, K., Otaka, M., Arai, T., Yoda, S., Nagai, S., Suzuki, T., Miura, T., and Karasawa, H.: "Development of Novel Visualization Technique of Flow Field for Liquid Metals Using High Temperature Ultrasonic Transducer," Proceedings of Fluid Measurements and Instrumentation, 2000 ASME Fluids Engineering Conference, FEDSM2000-11116 (2000) Boston.
[25] Karasawa, H., Izumi, M., Komai, M., Satou, N., Suzuki, T., Maruyama, M., Shioyama, S., Terashima, T., Nagai, S., Sasaki, S., and Uchikado, J.: "Development of Under Sodium Inspection Technique for FBR (2)," Proceedings of 5th International Conference on Nuclear Engineering (1997) Nice.
[26] Yasuhiro, S. and Imaishi, N.: "Numerical Simulation of Three Dimensional Oscillatory Marangoni Flow in Adiabatic Cylindrical Half-Zone Liquid Bridges" (NASDA-TMR-990007E) National Space Development Agency of Japan (1999) pp. 115-164.
[27] Sodeyama, K., Sakka, Y., Kamino, Y., and Hamaishi, K.: "Properties of Fine Shirasuballoons (in Japanese)," Journal of the Ceramic Society of Japan, Vol. 105 (1997) pp. 79-84.
[28] Sodeyama, K., Sakka, Y., Kamino, Y., and Seki, H.: "Preparation of Fine Expanded Perlite," Journal of Materials Science, Vol. 34 (1999) pp. 2461-2468.